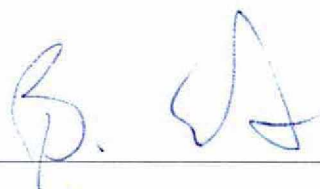# TRANSIENT SPATIOTEMPORAL CHAOS IN A MORRIS-LECAR NEURONAL RING NETWORK COLLAPSES TO EITHER THE REST STATE OR A TRAVELING PULSE

By

Keegan Keplinger

RECOMMENDED:

_____

_____

_____
Advisory Committee Chair

_____
Chair, Department of Physics

APPROVED:

_____
Dean, College of Natural Science and Mathematics

_____
Dean of the Graduate School

12/17/12
Date

TRANSIENT SPATIOTEMPORAL CHAOS IN A MORRIS-LECAR NEURONAL RING
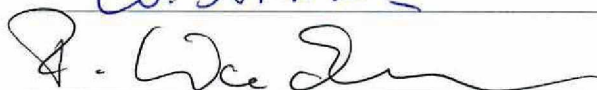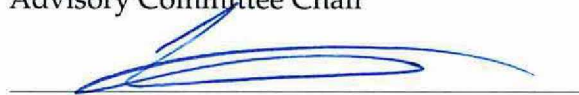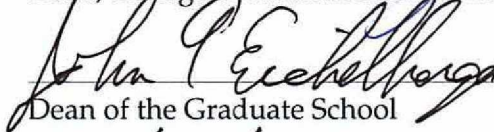NETWORK COLLAPSES TO EITHER THE REST STATE OR A TRAVELING PULSE

A

THESIS

Presented to the Faculty

of the University of Alaska Fairbanks

in Partial Fulfillment of the Requirements

for the Degree of

MASTER OF SCIENCE

By

Keegan Keplinger, B.S. Physics

Fairbanks, Alaska

December 2012

Abstract

Transient spatiotemporal dynamics exists in an electrically coupled Morris-Lecar neuronal ring network, a theoretical model of an axo-axonic gap junction network. The lifetime of spatiotemporal chaos was found to grow exponentially with network size. Transient dynamics regularly collapses from a chaotic state to either the resting potential or a traveling pulse, indicating the existence of a chaotic saddle. For special conditions, a chaotic attractor can arise in the Morris-Lecar network to which transient chaos can collapse. The short-term outcome of a Morris-Lecar ring network is determined as a function of perturbation configuration. Perturbing small clusters of nearby neurons in the network consistently induced chaos on a resting network. Perturbation on a chaotic network can induce collapse in the network, but transient chaos becomes more resistant to collapse by perturbation when greater external current is applied.

Table of Contents

List of Figures

Acknowledgements

Thanks to my wife, Aimee Fogler, for her supermaternal powers and unwavering support, to my daughter Vera Lynn, for her wild imagination, to my daughter, Darwin Linnae, whose character is blossoming, to my mother and father for, well, everything.

Thanks to my advisor, Renate Wackerbauer, for an outstanding exercise in quality control, to John Olson for many years of employment, funding, an unofficial advising, to my committee, Brian Edmonds and Vikas Sonwalkar, for their insights, to Barbara Taylor and Michael Harris for the opportunity to see the experimental side, to Channon Price and David Newman for their bizarre pedagogical approaches, to John Craven and Curt Szuberla just for the hell of it, to Mary Parsons and Sandy Jefko for gluing all the edges seamlessly together, and to many, many more whom I am too exhausted to remember.

"Insanity: doing the same thing over and over again and expecting different results."

—Albert Einstein

"Jump as quickly at opportunities as you do at conclusions."

—Benjamin Franklin

Chapter 1

Introduction

In 1999, the case was made for nonlinear dynamics in the neurosciences when Hugh Wilson published a (now out-of-print) textbook called *Spikes, Decisions, and Action* that explicitly emphasized the usefulness of nonlinear dynamics in understanding neural behavior[1]. In 2001, it was noted in Elsevier's *Current Opinion in Neurobiology* that nonlinear mathematical methods had crept into the field of neuroscience without much explicit acknowledgement despite having become pervasive in the field[2]. The language and behavior of many classes of dynamical systems are well-equipped to describe the majority of signaling behavior in neurons[3][1]. This seemingly esoteric field of study was named *neurodynamics* and eventually absorbed into the broader field of theoretical neuroscience[4], also known as mathematical neuroscience[5] or computational neuroscience[6]. Today, theoretical neuroscience institutes around the world are made up of mathematics, physics, computer science, electrical engineering, and neurobiology departments. Interdisciplinary teams work together to model and predict the behavior of neural systems.

Of particular interest in the nonlinear sciences is the relevance of transient dynamics to coupled neural systems. Significant transient behavior in neurons can occur on time scales from milliseconds to minutes and it is these transients that are thought to encode important information about stimuli in the environment[7]. This paper will briefly introduce the fundamental spiking mechanisms of the neuron and illustrate how complex, unpredictable behavior can emerge from a network of such diffusively-coupled neural elements. In particular, this paper will detail how a special case of chaos, transient spatiotemporal chaos, can collapse to produce both steady state and traveling wave solutions; a result demonstrated in few systems.

1.1 The Physics of Neurons

The physics of a neuron can, for many cases, be reduced to the interactions of three basic components: ions, a semipermeable membrane that separates concentrations of ions, and voltage-gated channels that allow passage of the ions across the membrane (Figure 1.1). More complex models may incur additional considerations, such as molecular network interactions and ligand-gated channels, but such accessions will be neglected here.
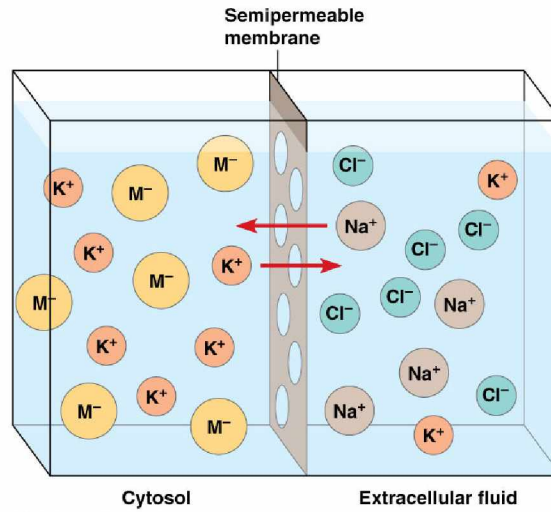
Figure 1.1. A semipermeable membrane separates two compartments of differing ion concentrations. Sodium (Na⁺), Chlorine (Cl⁻), Potassium (K⁺), and arbitrary proteins (M⁻) maintain a membrane potential. Channels in the membrane allow passage of Na⁺ and K⁺[8].

Neural circuits behave in a fundamentally different manner than traditional electronic circuits so the conceptual machinery required to understand neural spiking will be developed from a static condition. Consider an aqueous solution of a single species of ion in a container separated by a membrane partition. Two forces dominate interactions between the compartments. They are the electromagnetic force and the concentration gradient, the so-called driving force of diffusion. While the concentration gradient is not a mechanical force, it is helpful to think of the problem in terms of a force balance between diffusion and the electrodynamics. This concept was developed into a mathematical framework by Walther Hermann Nernst in the late 19th century in what has become known as the Nernst equation[9][10]:

$$E_n = \frac{RT}{zF} ln(Q).$$ (1.1)

E_n is the potential across the membrane, R is the universal gas constant, T the temperature, z the charge of the ion, F is the Faraday constant, and Q is the concentration gradient,

expressed as a ratio of concentrations between the two partitions. For a single ion species,

$$Q = \frac{[c]_E}{[c]_C},$$ (1.2)

where $[c]_C$ is the concentration in the cell, and $[c]_E$ is the concentration in the extra-cellular space. Notice that when the two partitions have the same concentration, $Q = 1$, giving $E_n = 0$. As ions are pumped from one membrane partition into the other and offset the concentration gradient, a nonzero electric potential is generated across the membrane. With the opening of an ion channel, the ions can flood back down the concentration gradient, generating a current. The currents generated in this fashion are the main component of the function of the neural compartment, but there is an additional caveat that makes neurons more dynamic: the system contains more than one ion species. Imagine now that the partitions have two ion species at different concentrations across the compartments. The general form of Equation 1.1 is retained, but for two ion species

$$Q = \frac{P_1[c^+]_E + P_2[c^-]_C}{P_1[c^+]_C + P_2[c^-]_E}.$$ (1.3)

This expression is known as the Goldman-Hodgkin-Katz equation. P_1 gives the permeability of the channel for a positive ion, $[c^+]_C$ the concentration of a positive ion in the cellular space (cytosol), $[c^+]_E$ the concentration of a positive ion in the extracellular space, P_2 the permeability of a negative ion and $[c^-]_C$ and $[c^-]_E$ the concentrations of a negative ion in the cytosol and extracellular space, respectively. The numerator of Equation 1.3 includes the sum of all positive charges from the extracellular space with the sum of all negative charges inside the cell, while the denominator sums the positive charges in the extracellular space and the negative charges from the cytosol. Each concentration is weighted by the permeability of the ion channel, which has a positive value for the open gate and equals zero when the gate is closed. Each of the ion species has a different Nernst potential (defined by Equation 1.1). Consider an open gate for the ion species with a higher Nernst potential. As it seeks equilibrium, the membrane potential spikes upward; the resulting higher membrane potential activates the second channel just as the first is reaching

the end of its time course. The first channel enters a refractory period where it cannot be excited by membrane potential. Meanwhile, the gate is open for the species with the lower Nernst potential, driving the membrane potential back downwards. As the second channel deactivates, the membrane returns to its resting potential, i.e., the effective resting potential determined by the collective concentrations of both ions, as described by Equation 1.3. The preceding series of events describes an *action potential*. As the neuron continues to fire, the concentration gradients are being slowly depleted. Biological systems have an internal pump that is constantly working to separate the charges so that the concentration gradients can be maintained. The channel gates, the pump, and the membrane can be described as electrical components in a circuit diagram (Figure 1.2) with the membrane acting as a capacitor, C_m, the pump acting as a current source, I_p, and the channel gates acting as non-ohmic conducting elements with conductance g_n and Nernst potential, E_n. Since real biological membranes are not perfect insulators, a general leak term, g_L, is added with Nernst potential E_L to represent a total effective leak through closed channels and the membrane itself.
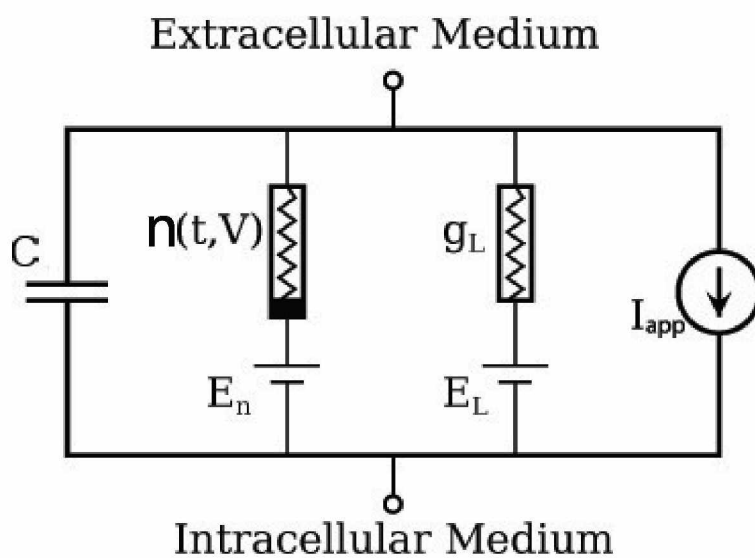

Figure 1.2. Circuit model for ion conduction with C the membrane capacitance, E_n the Nernst potential of the active channels, g_n the effective conductance of the active channels, E_L, the turn-around voltage for the leak channel, g_L the leak conductance, and I_{app}, the current of the ion pump.

Modeling a population of channels as they undergo gating over a distribution of times is not a trivial exercise. Spiking neuron models do not represent this process mechanistically, but rely on a set of empirically determined activation curves. These curves give the time course of channel population gating over time, mathematically represented by sigmoidal step functions such as the hyperbolic tangent function, $tanh(x)$. The first activation curves were determined in the 1950's by Alan Lloyd Hodgkin and Andrew Huxley[11]. Electrophysiology probes of the time were too large to get reliable readings from mammalian neurons, but the giant squid that were being caught off the east coast of the United States had axons large enough for the intracellular recordings that would eventually lead to a deeper understanding of neuronal discharge. Hodgkin and Huxley were the first to discover that it was a variety of ion species making up the action potential. They did so using channel blockers to separate an ion species' contribution to the total current. The dominant species in the dynamics of the mammalian neural system are Na^+ and K^+, with a Nernst potential of around $50mV$ and $-70mV$, respectively. A protein called sodium-potassium adenosine triphospate pump (Na^+ / K $^+$-ATPase) acts as the pump that maintains charge separation between the inside and the outside of the cell. Despite being developed from a squid axon, this general model applies to human and mammalian neurons and the four-dimensional *Hodgkin-Huxley model* is still the standard neuron model for investigating physiologically relevant questions about the nervous system. There are other ion currents in the neuron such as Ca^{2+} and Cl^- in addition to several subspecies of Na^+ and K^+ channels. As a result, many complicated permutations of the Hodgkin-Huxley model have been developed to describe particular examples of neural ensembles in nature, but the Hodgkin-Huxley model is not the only physiologically relevant neuron model.

In 1981, Catherine Morris and Harold Lecar developed the *Morris-Lecar model* based on the experimentally observed behavior of the barnacle giant muscle fiber[12]. The muscle fiber's primary currents are due to K^+ and Ca^{2+} (instead of Na^+) and the activation for the Ca^{2+} is considered instantaneous, thus no extra differential equation is required to describe population activation. Instead, it is a direct function of the membrane potential, V. This reduces the system two just two differential equations. One of them describes the change in membrane potential, the other describes the activation of the K^+ current. The derivation of the system begins with Kirchoff's current law for a circuit in the presence of an external

current, I_{app}. Explicitly, for an *isopotential patch* of membrane on the axon,

$$C\dot{V} + I_{Ca} + I_K = I_{app},\tag{1.4}$$

where C is the capacitance per area of the membrane and $\dot{V}$ is the change in membrane potential over time. The calcium current, I_{Ca} and the potassium current I_K are mediated by voltage sensitive gates; externally applied currents are represented by I_{app}. Currents are given relative to area, relating to the isopotential patch of membrane across which the membrane potential is considered. A particular ion species such as Ca^{2+} can be specified by its channel's maximum conductance per area (g_{Ca}), its Nernst potential (V_{Ca}), and the activation curve, $m_{ss}(V)$, determined by Morris and Lecar,

$$I_{Ca} = m_{ss}(V)g_{Ca}(V - V_{Ca}).\tag{1.5}$$

The activation curve is

$$m_{ss}(V) = (1 + \tanh(\frac{V - V_1}{V_2}))/2,\tag{1.6}$$

with V_1, the shift constant and V_2, the slope constant, fit to best match empirical data. The potassium current has associated with it an additional dimension to better represent the time-course of the channel population's gating response. Thus,

$$I_K = ng_K(V - V_K),\tag{1.7}$$

where n is the fraction of open gates for the entire channel population, g_K is the maximum conductance per area of the potassium channel, and V_K is the Nernst potential for potassium.

$$\dot{n} = \frac{n_{ss}(V) - n}{\tau_n(V)} \tag{1.8}$$

$$n_{ss}(V) = (1 + \tanh(\frac{V - V_3}{V_4}))/2 \tag{1.9}$$

$$\tau_n(V) = \phi \cosh(\frac{V - V_3}{2V_4}), \tag{1.10}$$

where n_{ss} is the activation curve for K$^+$, τ_n models the delay in the K$^+$ current, V_3 and V_4 are the shift and slope (respectively) of the activation curves, and ϕ is the reciprocal of the time constant associated with the delay function. Adding the leak current, I_L, the Morris-Lecar neuron model is given by

$$C\dot{V} = I_{app} - m_{ss}g_{Ca}(V - V_{Ca}) - ng_K(V - V_K) - I_L \tag{1.11}$$

$$\dot{n} = \frac{n_{ss} - n}{\tau_n}. \tag{1.12}$$

The Morris-Lecar model is a two-dimensional neuron model that can describe a wide variety of excitatory and oscillatory behavior.

1.2 Transient spatiotemporal chaos

Chaos has no universally accepted definition, according to Strogatz (1996), who gives the formal definition:

> "Chaos is *aperiodic long-term behavior* in a *deterministic* system that exhibits sensitive dependence on *initial conditions*."[13]

That is, the system must display long-term behavior that fits no consistent pattern, the system must only have one future trajectory for each point in phase space, and initial conditions that start arbitrarily close to each other diverge exponentially as the system evolves in time (Figure 1.3). The sensitivity to initial conditions can be quantified by the *Lyapunov exponent*, λ:

$$\lambda = \lim_{\substack{t \to \infty \\ d_0 \to 0}} \frac{1}{t} \ln \left[\frac{d(t)}{d_0} \right], \qquad (1.13)$$

the logarithm of the distance, $d(t)$, between two trajectories that started a distance, d_0, in state space, normalized by the time span, t, over which the trajectories evolved. The Lyapunov exponent is defined as d_0 approaches zero and as t approaches infinity. Bounded, nonlinear systems with a positive Lyapunov exponent are considered chaotic. Linear systems are excluded, as they can have a positive Lyapunov exponent without demonstrating the irregular long-term patterns that characterize chaos.
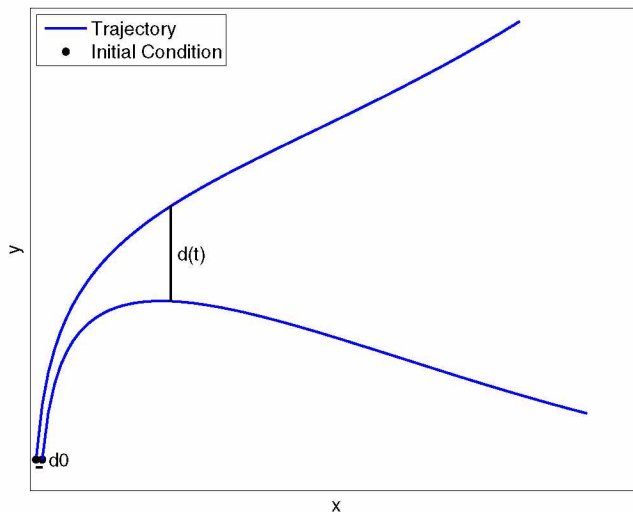

Figure 1.3. Exponential sensitivity to initial conditions. Two trajectories (black stars) begin arbitrarily close to each other but diverge exponentially in phase space (black lines).

Transient chaos is a class of chaos whereby deterministic systems exhibit chaotic behaviour for a finite time period before collapsing to an *attractor*, such as a steady state or limit cycle. Attractors are invariant sets in a bound system that attract an open set of initial conditions[13]. Trajectories experiencing transient chaos can be found in the neighborhood of an invariant set, called a *chaotic saddle*[14]. Transient chaos is opposed to *asymptotic chaos*, in which trajectories exist on the *chaotic attractor* and system collapse never occurs. A typical example of asymptotic chaos exists in some regions of parameter space in the Lorenz

system [15]. The chaotic attractor has only stable manifolds, while the chaotic saddle has both stable and unstable manifolds. In physical systems, transient chaos is typically a consequence of chaotic saddles[14]. A simple example for which transient chaos exists is the tent map (Figure 1.4):

$$x_{n+1} = \begin{cases} \mu x_n & \text{for } 0 \leq x < \frac{1}{2} \\ \mu(1-x_n) & \text{for } \frac{1}{2} \leq x \leq 1. \end{cases} \tag{1.14}$$
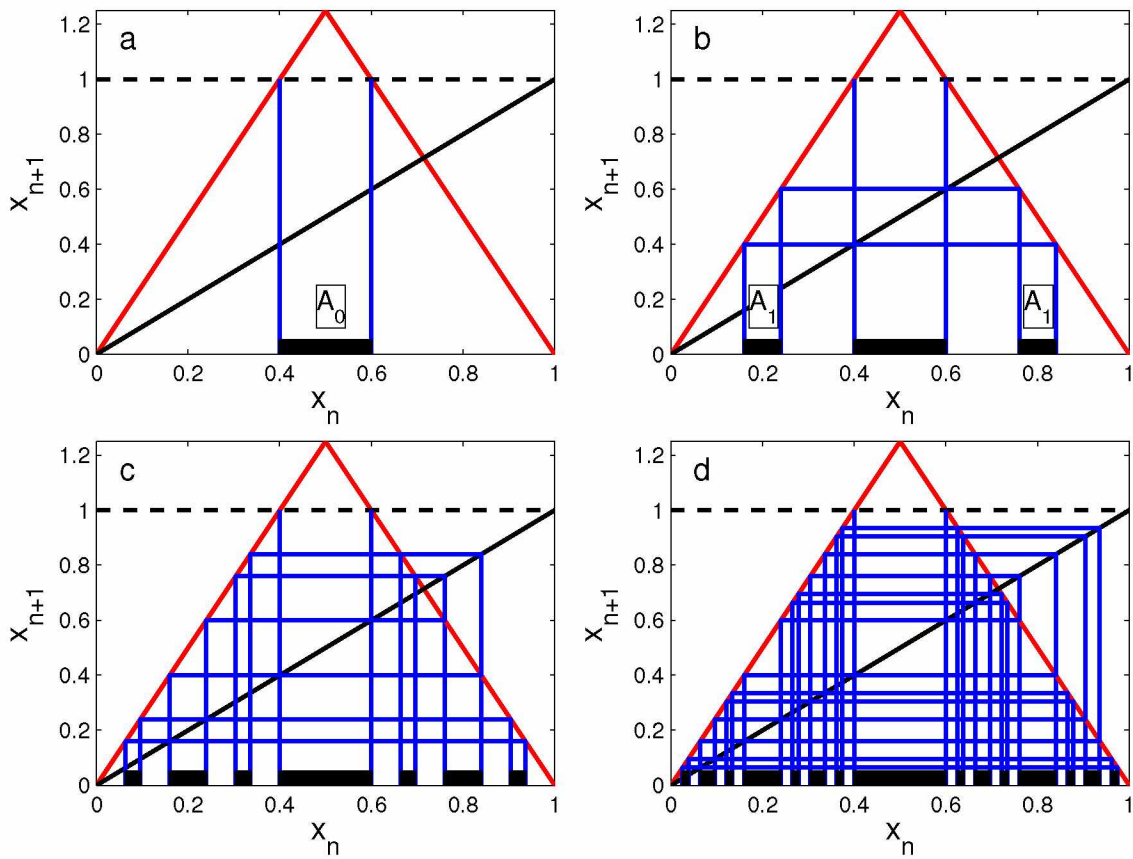

Figure 1.4. Trajectories of the tent map with $\mu = 2.5$ for a) n=0, b) n=1, c) n=2, d) n=3. Trajectories (blue line) escape when $x_{n+1} > 1$ (dashed black line). The range of x_n contains continuous intervals of escape (thick lines) for each n. $x_{n+1} = x_n$ (sloped solid black line) shows the iteration step.

The tent map is non-invertible; for each state, x_n, there are two preimages, x_{n-1}. For $\mu > 2$, trajectories can escape the unit interval $\iota = [0,1]$ when $x_{n+1} > 1$. For initial conditions $x_0 \in A_0 = (\frac{1}{\mu}, 1 - \frac{1}{\mu})$, the trajectory immediately escapes the interval (Figure 1.4a). The initial conditions $x_0 \in A_1 = (\frac{1}{\mu^2}, \frac{1}{\mu} - \frac{1}{\mu^2}) \cup (1 - \frac{1}{\mu} + \frac{1}{\mu^2}, 1 - \frac{1}{\mu^2})$ require one more iteration to escape the interval, ι (Figure 1.4b). Similarly, the endpoints of each interval in A_1 have two preimages, giving four intervals that make up A_2 (Figure 1.4c). Initial conditions starting on A_2 escape in two iterations, and so on. Taking, the length of A_0 to be $L(A_0) = \frac{2-\mu}{\mu}$ and generalizing this process, for the number of iterations required to escape, m, there exists 2^m intervals of size $Ł(A_0) \cdot (\frac{1}{\mu})^m$ that together make up the region of escape, A_m. With this in mind the length, $Ł_e$, of this escape region is given by

$$Ł_e = Ł(A_0) \sum_{m=0}^{\infty} \left(\frac{2}{\mu}\right)^m. \tag{1.15}$$

This expression evaluates to $Ł_e = 1$, equal to the length of the interval the tent map is defined on. The remaining points define the invariant manifold of length zero called the Cantor set (Figure 1.5). In the tent map, this collection of points defines the *chaotic repeller*, an analogy to the chaotic saddle for non-invertible maps. This result implies that the chance of a randomly selected initial condition starting on the invariant manifold is zero.
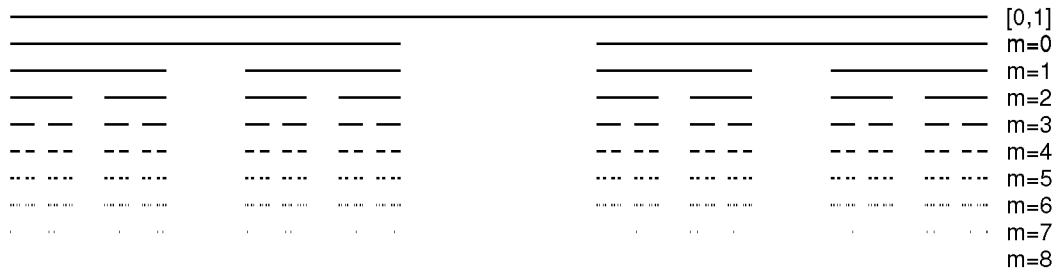

Figure 1.5. The cantor set. Successive removal of A_m from the interval $[0,1]$ in the tent map for the integers $0 \le m \le 8$ with $\mu = 2.5$.

A dynamical system can be extended spatially by coupling multiple dynamical elements (such as neurons) together. If the dynamics of the coupled system displays sensi-

tivity to initial conditions ($\lambda > 0$) the behavior is called *spatiotemporal chaos*. Mechanisms have been proposed for spatiotemporal chaos[16][17][18], but *transient spatiotemporal chaos* is a relatively recent discovery. The collapse process of such large ensembles of coupled elements remains obscured by their high dimensionality, but noise[19] and nonlocal coupling[20] can influence the time-course of transient chaos. Because the transient behavior in spatiotemporal systems can exist for long periods of time, it is sometimes difficult to determine whether chaotic dynamics is asymptotic or transient[21], but methods for determining the differences between the two classes of chaos are under development[22].

In the biological sciences, spatiotemporal chaos has found applications in cellular automation[23], slime mold chemotaxis[24], infected plankton[25], and other population models[26][27][28]. Spatiotemporal chaos has also been demonstrated in several neuron models[29][30][31] and applications to information processing[32][33] may give insights into how cognitive processes correlate with neural system dynamics. The existence of transient spatiotemporal chaos in biological systems is unexplored.

Neurons are often modeled as *excitable* systems, for which there is a threshold. For subthreshold perturbations, the system returns immediately to the steady-state attractor until acted on by another perturbation. Perturbations that surpass the threshold cause the system to undergo an *excitation cycle* before returning to the steady-state attractor.

A typical class of spatiotemporal systems that host transient spatiotemporal chaos are *reaction-diffusion systems*[14][34][35][36] in which excitable elements are coupled spatially through a diffusion term. A network of diffusively-coupled neurons represents electrically-coupled networks in the nervous system called *gap-junction* networks. The role of these electrical synapses in neural computation have long been under-appreciated[37]. In electrical signaling aspects, gap junctions were thought to serve little more functionality than synchronization in electrical signaling[38], but evidence is growing that demonstrates a more significant role for gap junctions, such as enhancing the dynamic range of retinal neurons[39] and the generation of bursting oscillatory behavior[40]. *Axo-axonic* gap-junctions have unique anti-dromic properties that, experiments suggest, lend to the excitability of inhibitory GABA neurons in the hippocampus[41]. They've also been found to allow for faster interneuron spike propagation that participates in neural networks independent of the afferent flow of chemical synapses. This unique functionality is hypoth-

esized to explain memory consolidation in the hippocampus where axo-axonic gap junctions are present[42]. The dynamical properties of such a diffusively-coupled network of axons will be explored with the goal of contributing to the computational aspects of gap junctions in nature as well as to the general understanding of the mechanisms involved in the collapse of transient spatiotemporal chaos.

1.3 Synopsis

Chapter 2 presents the spatially extended Morris-Lecar neuron system, the parameter region of interest, and its biological relevance.

Chapter 3 demonstrates the existence of transient spatiotemporal chaos in the Morris-Lecar network with lifetimes that increase exponentially as a function of network size. The system dynamics can collapse onto three types of attractors after long periods of transient chaos including a global steady-state attractor, a pulse-state attractor, or a chaotic attractor.

In Chapter 4, transient behavior is studied as a function of initial condition to develop an understanding of the typical perturbation required to induce chaos in the Morris-Lecar network.

Chapter 5 explores how perturbations facilitate the collapse of spatiotemporal chaos in the Morris-Lecar network.

Chapter 6 provides general conclusions and an outview. Possible applications to neurobiology and the nonlinear sciences are discussed, and future research on the diffusively-coupled Morris-Lecar network is proposed.

Chapter 2

Model

The Morris-Lecar neuron model is similar to the four-dimensional Hodgkin Huxley neuron model, but has only two dimensions which describe the membrane potential, V, and calcium channel population state, n. The model displays both Type 1 (integrator) and Type II (resonator) neural behaviors, depending on selected parameters. Here, a Type I parameter regime is employed. A feedback-coupled ring network topology is implemented with each node representing a Morris-Lecar neuron, an empirically determined ion current model of the barnacle giant muscle fiber[12].The ith neuron in the spatially extended Morris-Lecar system is described by

$$\dot{V}_i = \frac{1}{C}[I_{app} - f(V_i, n_i)] + D[V_{i+1} + V_{i-1} - 2V_i] \qquad (2.1)$$

$$\dot{n}_i = \frac{n_i - n_{ss}(V_i)}{\tau_n(V_i)} \qquad (2.2)$$

with

$$f(V_i, n_i) = I_L + I_{Ca} + I_K \qquad (2.3)$$

and

$$I_L = g_L(V - V_L) \qquad (2.4)$$

$$I_{Ca} = g_{Ca} m_{ss}(V - V_{Ca}) \qquad (2.5)$$

$$I_K = g_K n(V - V_K). \qquad (2.6)$$

The activation curves are defined by their steady state sensitivity to voltage,

$$m_{ss} = \frac{1}{2}(1 + \tanh[\frac{V - V_1}{V_2}]) \qquad (2.7)$$

$$n_{ss} = \frac{1}{2}(1 + \tanh[\frac{V - V_3}{V_4}]) \qquad (2.8)$$

$$\tau_n = \frac{1}{\varphi \cosh[\frac{V - V_3}{2V_4}]}. \qquad (2.9)$$

These expressions describe the leak, calcium, and potassium currents, I_L, I_{Ca}, and I_K as well as the activation curves, m_{ss} and n_{ss}, and the potassium delay function, τ_n. The parameters for this paper include the coupling constant, $D = 0.05\mu S/(\mu F \cdot cm^2)$, chosen for its rich dynamics, as well as the experimentally-determined parameters[12] for each Morris-Lecar neuron in the network: membrane capacitance, $C = 20uF/cm^2$, the maximum conductance of the potassium channel, $g_K = 8uS/cm^2$, the maximum conductance of the Ca^{2+} channel, $g_{Ca} = 4uS/cm^2$, the leak conductance, $g_L = 2uS/cm^2$, the Nernst potential of the K^+ current, $V_K = -80mV$, the Nernst potential of the Ca^{2+} current, $V_{Ca} = 120mV$, the Nernst potential of the leak current, $V_l = -60mV$ and time constant, $\varphi = \frac{1}{15}Hz$. Fitting constants for the hyperbolic functions include $V_1 = -1.2mV$, $V_2 = 18mV$, $V_3 = 14.95mV$, and $V_4 = 17.4mV$.

For the parameter range of interest, linear stability analysis reveals three equilibrium points in the system to be a stable fixed point, a saddle point, and an unstable focus (Figure 2.1). A typical excitation cycle (dashed line) passes around the unstable focus and returns to the global steady state. The applied current acts as the bifurcation parameter, $I_{app} \in [28.1, 38]mA/cm^2$. In this parameter range, the Morris-Lecar system experiences a saddle-node bifurcation when $I_{app} \approx 38.8mA/cm^2$, giving rise to a stable limit cycle (Figure 2.2). Near $I_{app} = 42mA/cm^2$, a subcritical Hopf bifurcation arises as the unstable focus becomes stable and an unstable limit cycle is born. An in-depth bifurcation analysis was performed by Tsumoto[43] in which several bifurcation parameters were selected. The Morris-Lecar neuron behaves as an excitable system for applied currents below the saddle-node bifurcation. As the applied current exceeds the bifurcation point, a stable limit cycle is born leading to persistent oscillatory behavior. In the coupled ring system, an applied current of $I_{app} \geq 28.1mA/cm^2$ is required for excitability to propagate beyond the first excited neuron if all other neurons are initially at their resting potential.
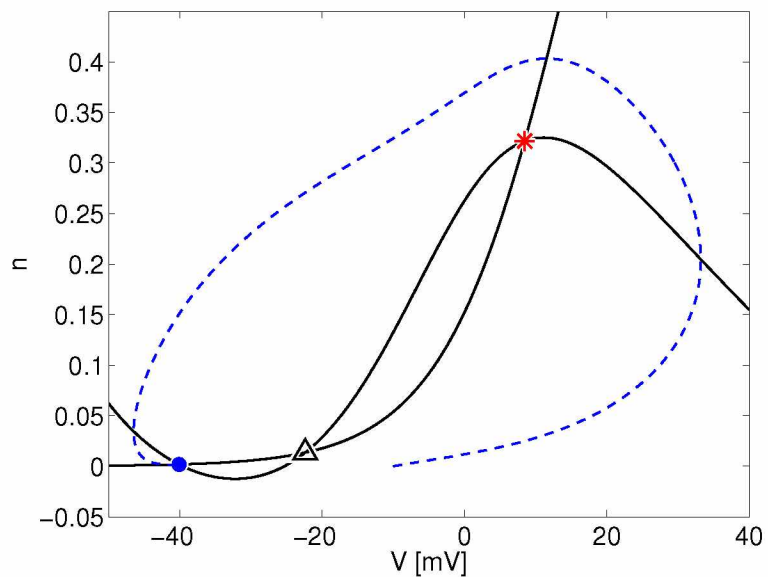
Figure 2.1. Phase diagram of the Morris-Lecar system. The membrane potential, V, is plotted against the fraction of K$^+$ channels open, n, for an isopotential patch of membrane. Linear stability analysis reveals a stable node (round dot), a saddle node (triangle), and an unstable focus (star). A typical trajectory makes an excitation around the unstable focus (dashed line). The bifurcation parameter is $I_{app} = 32mA/cm^2$, within the excitable regime of the Morris-Lecar system.
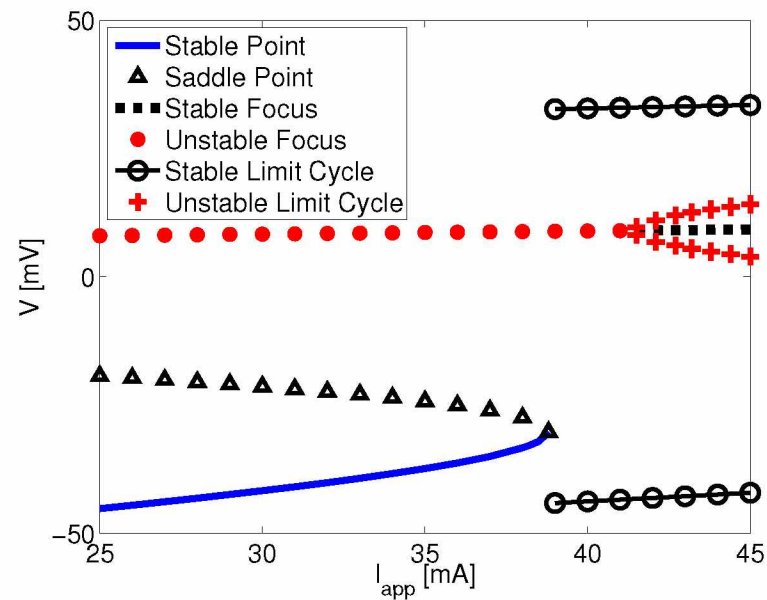
Figure 2.2. Bifurcation diagram for the membrane potential, V, as a function of bifurcation parameter, I_{app}. In the parameter range of interest, a saddle-node bifurcation occurs as the stable node (solid line) and saddle point (triangles) collide ($I \approx 38.9 mA/cm^2$), accompanied by the birth of a stable limit cycle (circle-line) about the remaining unstable focus (dots). The limit cycle is represented by the extrema of V. When $I_{app} \approx 41 mA/cm^2$, the unstable focus (dots) becomes stable (dashed line), leading to a subcritical Hopf bifuraction with an unstable limit cycle (pluses).

Chapter 3

Transient spatiotemporal chaos

Complex spatiotemporal dynamics were investigated in the electrically coupled Morris-Lecar network in the range $28.1mA/cm^2 \leq I_{app} \leq 38mA/cm^2$ with a coupling strength of $D = 0.05\mu S/(\mu F \cdot cm^2)$. Irregular spatiotemporal patterning exhibits different characteristics across the range of the bifurcation parameter. For $28.1mA/cm^2 \leq I_{app} < 28.3mA/cm^2$, pulse solutions do not exist and the direction of wave excitation can reverse, presumably as a result of instabilities at the trailing end of a wave pulse (Figure 3.1a). When $I_{app} \geq 28.3mA/cm^2$, the network emits pulse trains (Figure 3.1b). The network becomes dominated by activity for $I_{app} \geq 32mA/cm^2$ as more current is injected into the system (Figure 3.1c). Spatiotemporal structures continue to develop for higher currents (Figure 3.1, c and d). In this regime, local oscillatory events (white beads) can develop and interact over time, causing local collapse events (white triangular structures) that end in another bead of oscillatory events, a behavior indicative of computational roles for gap junction networks. Subtle, persistent ripple-like structures resemble neural bursting behavior where the network is active (darker color) and trajectories spiral away from the unstable focus. Phase plots for these three cases, for $I_{app} = 38mA/cm^2$, are given in Figure 3.2. For $I_{app} < 28.1mA/cm^2$ the network is not excitable despite individual neurons being excitable. As the applied current is increased above $38mA/cm^2$, the birth of a limit cycle in individual neurons gives rise to persistent oscillations in the network. Adjusting the coupling constant, D, of the network can alter the range of applied current over which transient chaotic dynamics exist, increasing the range with increased D. Changes in the coupling constant can also have an effect on the qualitative appearance of spatiotemporal structures during spatiotemporal chaos.

The network is initiated with most of the neurons at the resting potential. A random set of *input neurons* are selected and perturbed to a membrane potential of $-10mV$, sufficient to excite the neuron around the unstable focus (Figure 2.1). For $I_{app} < 30mA/cm^2$, a larger set of input neurons is required to induce complex spatiotemporal dynamics with sufficient probability. As I_{app} approaches the saddle-node bifurcation, the number of input neurons required to induce chaos is reduced to one.

After short-term transients have settled, convergence to a positive maximum Lyapunov
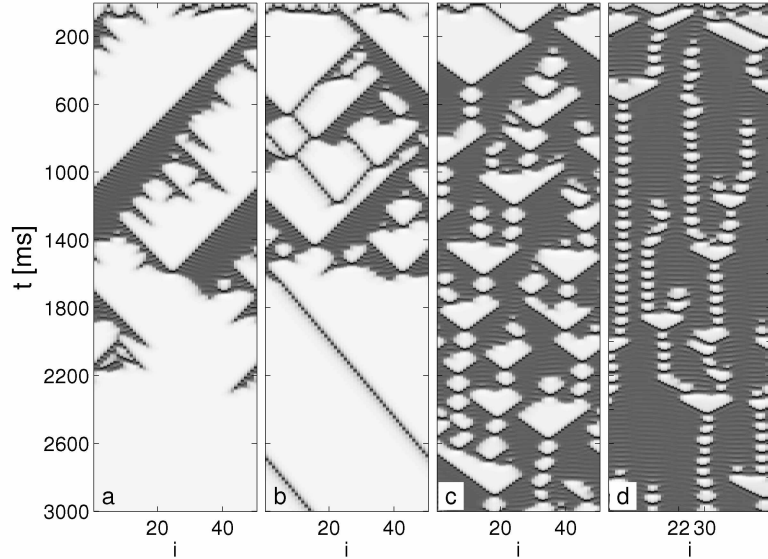
Figure 3.1. Complex spatiotemporal dynamics in the Morris-Lecar ring network for an applied current of a) $28.1mA/cm^2$, b) $28.5mA/cm^2$, c) $32mA/cm^2$, and d) $38mA/cm^2$. Colors indicate when the membrane potential, V, is at rest potential (white) or exhibiting burst-like activity (black) near the focus. All neurons in the 50-neuron network are initially at the resting potential with the exception of 10 randomly selected input neurons set to $(V, n) = (-10mV, 0)$.

exponent is measured, using methods developed by Giancarlo Benettin[44]. The Lyapunov exponent grows with network size, converging near a network size of 500 neurons (Figure 3.3a). An increase in the bifurcation parameter, however, reduces the Lyapunov exponent (Figure 3.3b) as the patterns become more oscillatory (Figure 3.6d). For $I_{app} \in [28.1, 28.5]mA/cm^2$, chaos is short-lived (Figure 3.3b).

After a period of transient spatiotemporal chaos, the dynamics typically collapses to either the steady state (Figure 3.4a) or a pulse solution (Figure 3.4b). With the exception of some uncommon cases near $I_{app} = 38mA/cm^2$, all sets of initial conditions will eventually result in a collapse to either one of these two attractors.

As the individual neurons of an ensemble become closer to each other in their projected phase state, they approach a homogenous state. When all neurons in the network have a membrane potential anywhere below their firing threshold at the same moment, the dynamics of the network collapses to the rest state. The degree of homogenity in the network
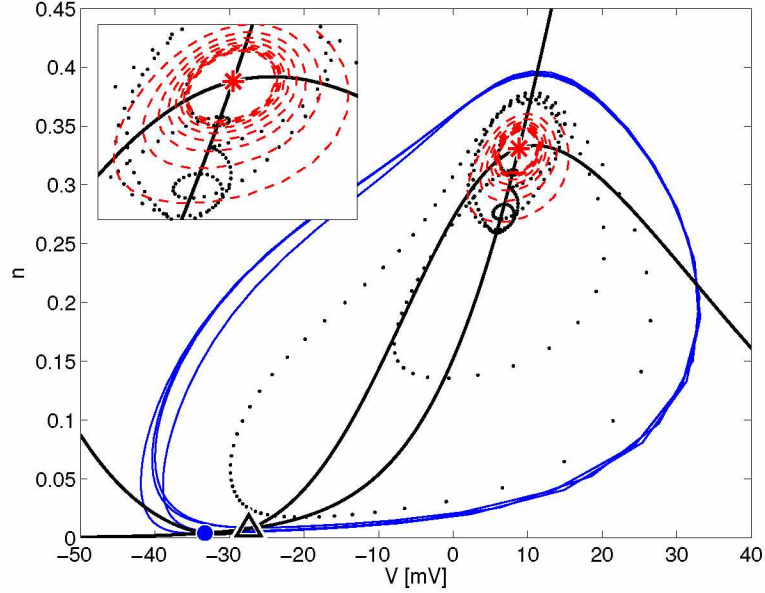
Figure 3.2. Typical trajectories for individual neurons in the network. Three basic dynamics are classified from Figure 3.1d: oscillations (blue line) from neuron $i = 30$, burst-like behavior (red dashed line) from neuron $i = 22$, and a neuron in between these two (black dotted line). Inset: a closer look at the unstable focus, where trajectories spiral away.

is measured with Kuramoto's order parameter[45] by taking the unstable focus (Figure 2.1) to be the origin of the coordinate frame and transforming trajectories from cartesian coordinates, (V, n), to polar coordinates, (ρ, ϕ). As a function of the phase, ϕ, the mean field is defined

$$\mathbb{Z} = \frac{1}{N} \sum_{i=1}^{N} e^{j\phi_i}, \tag{3.1}$$

where N is the size of the network, and ϕ_i the phase of neuron i. $\mathbb{Z}$ is a complex number with phasor notation $Re^{j\theta}$. Synchronization measures in this paper rely only on the amplitude of the order parameter, $R \in [0, 1]$. When the network is completely homogenous, all neurons share the same phase, and $R = 1$. As the phase of individual neurons diverge from each other, $R \to 0$. During chaotic behavior in the Morris-Lecar network, the order parameter approaches $R = 1$ several times before collapsing (Figure 3.5b), indicating
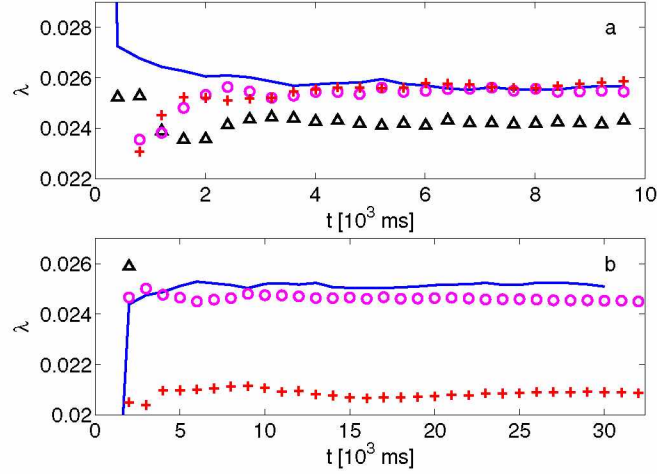
Figure 3.3. a) A positive maximum Lyapunov exponent, λ, was calculated as a function of network size, N equals 100 (triangles), 500 (solid line), 1000 (circles), and 2000 (pluses). b) A positive maximum Lyapunov exponent is measured for varying applied current, I_{app}, of $28.5mA/cm^2$ (triangles), $30mA/cm^2$ (solid line), $35mA/cm^2$ (circles), and $38mA/cm^2$ (pluses). The Lyapunov exponent is measured with a sampling rate of $\delta t = 0.1$ ms using an initial distance, $d_0 = 0.01$ mV between initial conditions.

a spontaneous and unpredictable collapse.

The lifetime of chaotic behavior preceding a collapse grows exponentially with network size (Figure 3.6a) as is typical of transient chaos in reaction-diffusion systems [35, 36]. Whether the final state after collapse was a pulse solution or steady-state solution has no significant relationship with how long the network remained active. The distribution of lifetimes for pulse and steady-state collapse do not differ significantly from each other in mean or standard deviation (Figure 3.6a,b). The probability of a collapse to the pulse state, p_P, increases with network size. For all network sizes, the probability of a pulse solution, p_P, as a function of applied current consists of an early peak at $I_{app} = 28.5mA/cm^2$ and a later peak at $I_{app} = 35mA/cm^2$ (Figure 3.6c).

Near $I_{app} = 38mA/cm^2$, an asymptotic attractor appears in the Morris-Lecar system. In the bifurcation diagram of a single Morris-Lecar neuron, the parameter is near the saddle-node bifurcation where the limit cycle is born (Figure 2.2). When the system collapses from the transient chaotic state to an asymptotic chaotic state, the Lyapunov exponent drops dramatically from $\lambda \approx 0.021$ to $\lambda \approx 0.006$. The short time Lyapunov exponent shifts
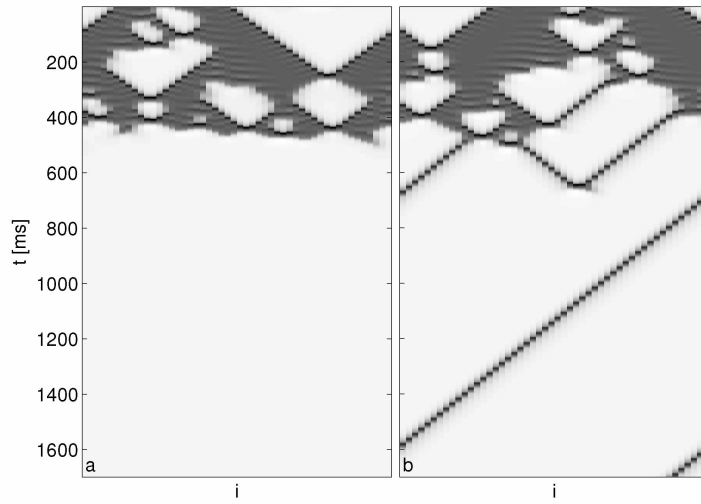
Figure 3.4. Collapse of Chaos. Spatiotemporal dynamics of membrane potential, V, during collapse for two different initial conditions in a 50-neuron network with $I_{app} = 30mA/cm^2$. The network collapses to the a) steady-state and a b) pulse solution. Refer to Figure 3.1 for technical details.

from an irregular temporal pattern to rhythmic one (Figure 3.7a).

The asymptotic chaotic spacetime structures exhibit small isolated clusters of neurons with a temporal rhythm that appears regular and periodic by eye, but has a positive Lyapunov exponent. An arbitrarily small perturbation on the network will dislodge the dynamics from the chaotic attractor, leading to transient chaos (Figure 3.8). The asymptotic chaos state is most common in networks of size, $N = 20M$ (where M is in an integer) in which $2M$ oscillating clusters develop at a distance of ten neurons. Burst-like activity dominates the rest of the network. The same result can be achieved by taking a network of size $N = 20M$ at rest and perturbing every 20th neuron in the ring network; for example, a 20-neuron network would require only a single neuron excited for which two oscillating neuron clusters develop, one at the perturbation point and one where the left and right traveling waves meet at the other side of the network from the input neuron. Asymptotic chaos can exist for other network sizes, but rarely occurred in random trials.

In the given bifurcation parameter range, the Morris-Lecar network demonstrates transient spatiotemporal chaos that can collapse to two attractor states, the steady-state and the pulse state. For larger applied currents, near the saddle-node bifurcation, a chaotic
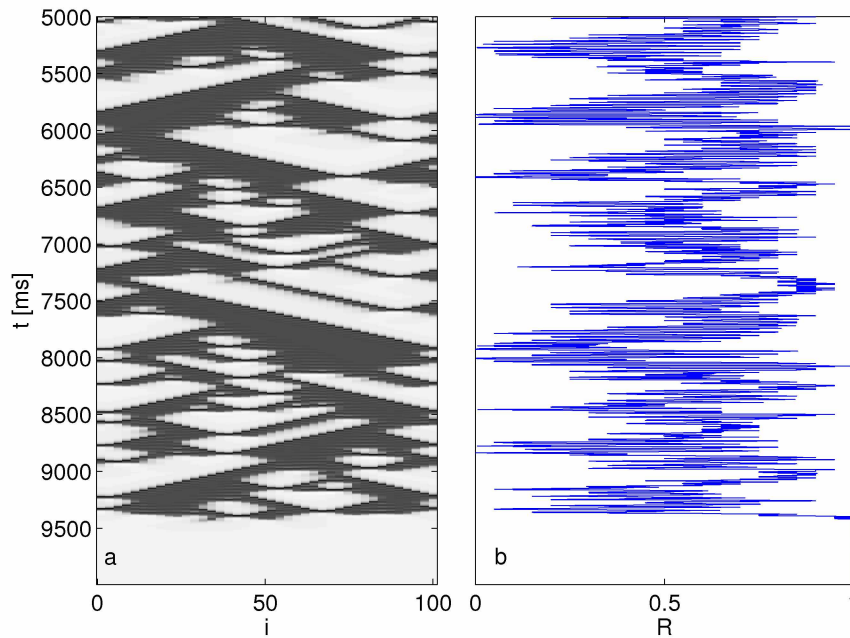
Figure 3.5. Order parameter. a) Spatiotemporal collapse in a 40-neuron network with $I_{app} = 28.3mA/cm^2$. Refer to Figure 3.1 for technical details. b) The order parameter, R, for the spatiotemporal dynamics in a).

attractor arises in the system. For special initial conditions, and for approximately 10% of lifetime trials for network size $N = 20, 40$, trajectories collapse from the chaotic saddle to the chaotic attractor. The collapse of transient spatiotemporal chaos is not predicted by the order parameter, but statistics demonstrate an exponential increase in the lifetime of transient chaos with network size and applied current.
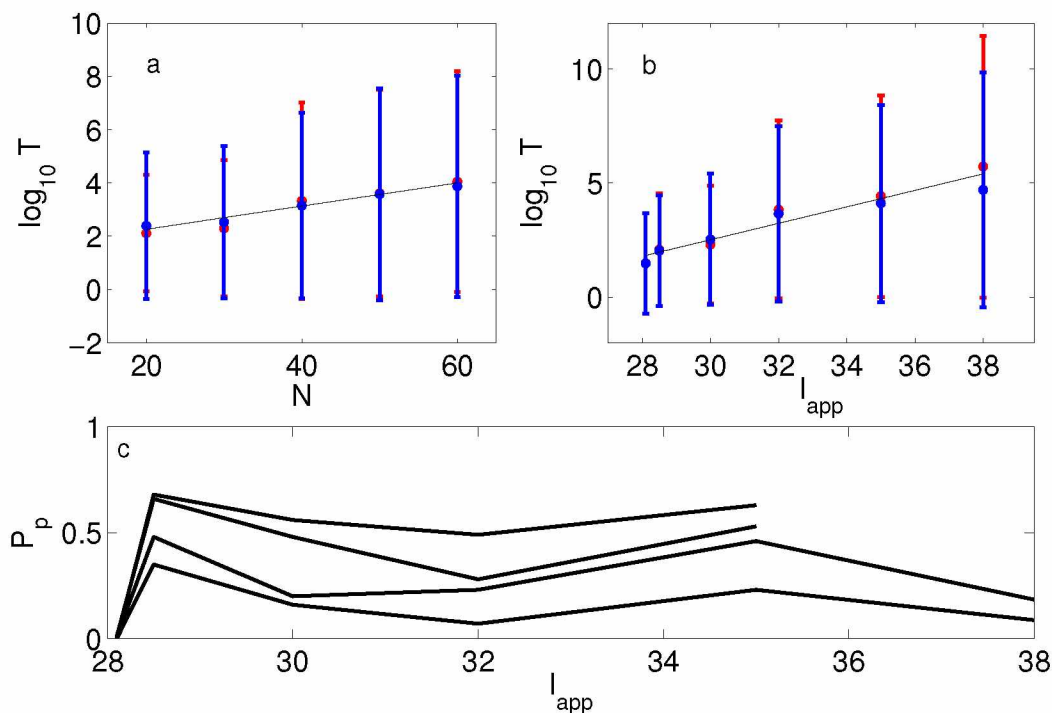
Figure 3.6. Lifetime analysis. a) Exponential growth in the average lifetime of transient chaos, T, as a function of network size, N for $I_{app} = 30mA/cm^2$. b) Exponential growth in T as a function of applied current, I_{app} for $N = 30mA/cm^2$. c) Percent of lifetimes that collapsed to a pulse state, P_p, as a function of I_{app} for $N = 20, 30, 50,$ and 60 (ascending). Missing points at $I_{app} = 38mA/cm^2$ due to long computing times and trouble distinguishing asymptotic chaos from transient chaos in an efficient, algorithmic matter. Statistics gathered from 100 trials on a 100-neuron network initiated with $0.8N$ neurons in the rest state and $0.2N$ input neurons at $(V, n) = (-10mV, 0)$. All cases collapsed to either the steady-state (blue bars) or the pulse solution (red bars) with the exception of $I = 38mA/cm^2$ in which $\approx 10\%$ of solutions ended in an asymptotic chaotic state.
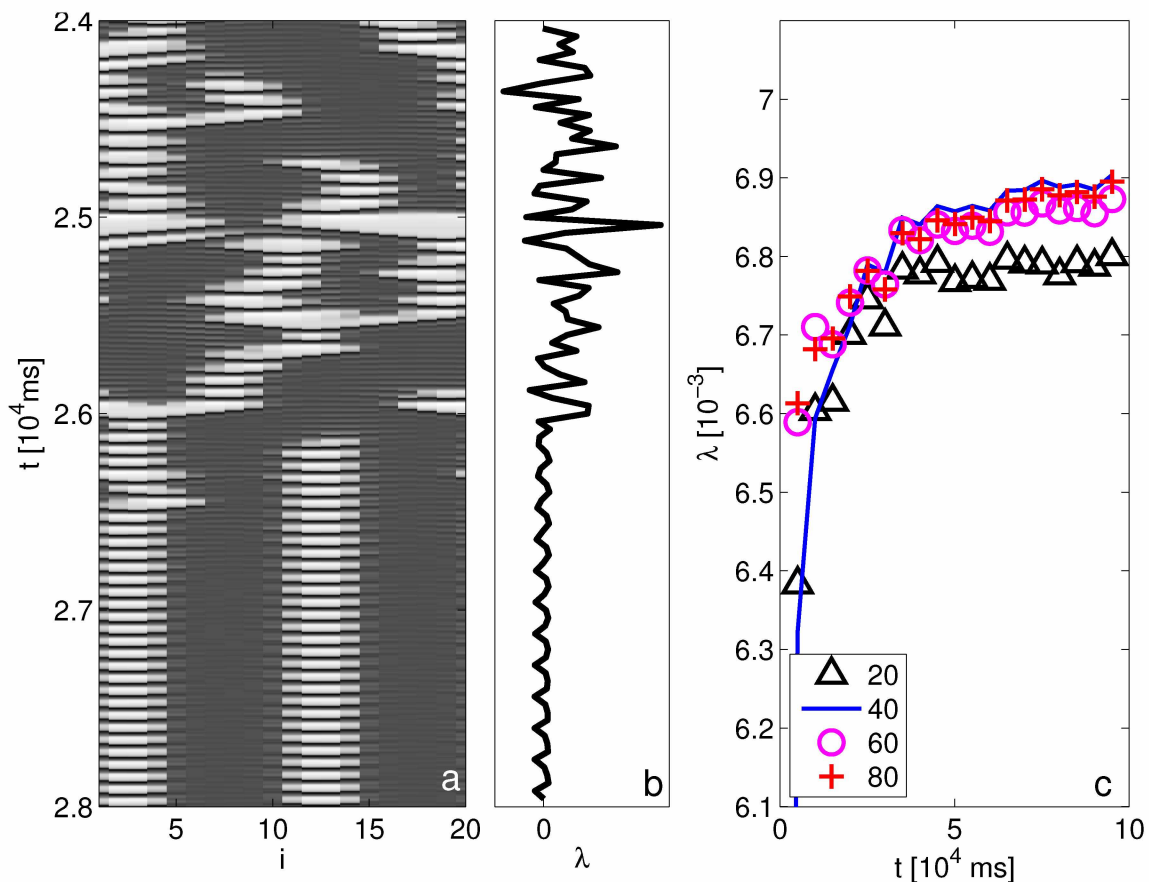
Figure 3.7. Asymptotic chaos. a) The collapse of transient spatiotemporal chaos to a chaotic attractor for $I_{app} = 38mA/cm^2$ and $N = 20$. Refer to Figure 3.1 for technical details. b) The short-time Lyapunov exponent of the collapsing dynamics, λ, over time, t. The short-time Lyapunov constant is measured in the same way as the long-term Lyapunov exponent (details in Figure 3.3) but every $10ms$ are calculated independently of preceding Lyapunov measurements. c) The Lyapunov exponent of the asymptotic chaotic state at $I_{app} = 38mA/cm^2$ for a variety of network sizes. Sample time for measurements ($\delta t = 0.1ms$) are significantly smaller than the time required for the dynamics to transition to the neighborhood of the chaotic saddle.
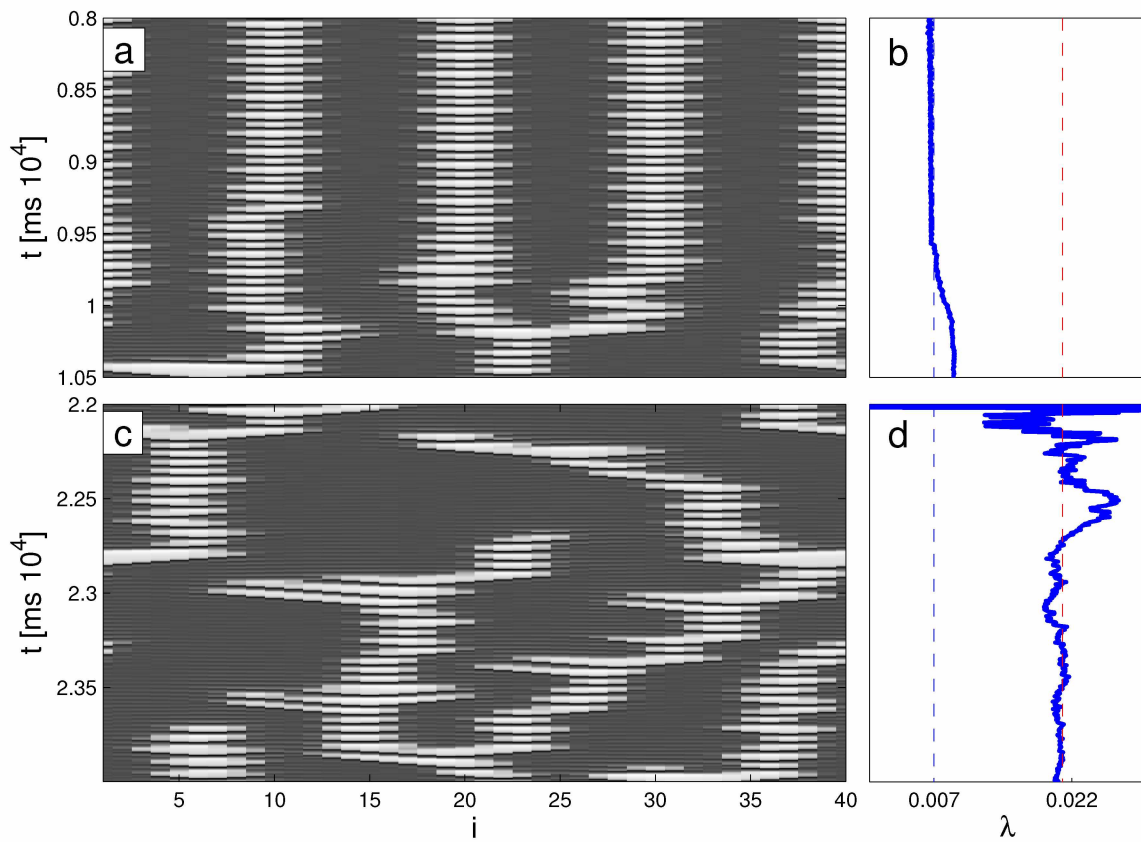
Figure 3.8. a) Perturbations on the chaotic attractor induce transient chaos for $I_{app} = 38mA/cm^2$. Refer to Figure 3.1 for technical details. b) The Lyapunov exponent begins to climb away from $\lambda = 0.007$ (blue dashed line). c) Spatiotemporal dynamics around $10^4 ms$ after the perturbation. d) Lyapunov exponent converging on $\lambda = 0.021$ (red dashed line) for the network perturbed in a). See Figure 3.3 for technical details about Lyapunov calculation.

Chapter 4

Perturbations on a network at rest

It has been stressed through both experiment and theory in recent years that the emphasis for a dynamical systems approach to brain function must be broadened to include not just the attractor states, but the transient states of biological neural networks [46, 47, 48]. In particular, it has become desirable to understand the nature of the transient states that connect attractors[7]. As demonstrated in Section 3, the path from transient chaos to an attractor is deterministic and requires no external perturbation. However, nervous systems are often subject to external stimuli which can dislodge the network from its attractors, giving the system a path back to the transient state.

With this in mind, we investigate how the strength and spatial distribution of a perturbation affects the network's transient path. Three network states are considered: the *steady-state attractor*, a *pulse state attractor*, and a *chaotic state*. The network is initialized on the steady-state attractor and a perturbation is introduced. After a finite time period, L, the network's state is measured. The information is recorded in a basin-like plot that demonstrates the relationship between perturbations and the instantaneous state of the network. The time period and measurement process are designed such that trajectories perturbed from the steady-state attractor go immediately to the pulse-state are recorded as pulse-state, while trajectories that fall immediately back to the steady-state attractor are recorded as steady-state. If a trajectory develops spatiotemporal chaos before collapsing to the steady-state within the measurement period, L, it is marked as chaotic state. The purpose of this study is to understand the pathway from the steady-state attractor to chaos through perturbation.

For a network of 100 neurons, the phase space is 200-dimensional with two dimensions for each of the 100 neurons. Thus, an abstraction is used to represent all 100 initial neuron states in the two rudimentary dimensions, V and n of a single neuron. A single neuron is selected as the input neuron and set to each discrete point in the phase portrait. The network then evolves deterministically for $L = 1000ms$ when the state of the network is determined. The *instantaneous network state* (INS) is represented by a colored pixel at the phase point of the input neuron (Figure 4.1). The basin-like plot shows for which configuration of input neurons the network dynamics reached the neighborhood of the chaotic

saddle. For most cases, the network returned immediately to the steady-state where it was initially perturbed from. There is, however, a region of excitability for which the network dynamics become caught in the region of the chaotic saddle or the pulse-state attractor. States that get caught immediately on the pulse-state attractor without exhibiting transient chaos are recorded as pulse states (Figure 4.2). If trajectories reach the neighborhood of the chaotic saddle before collapsing onto the pulse state, they are reported as a chaotic state in the basin-like plots.
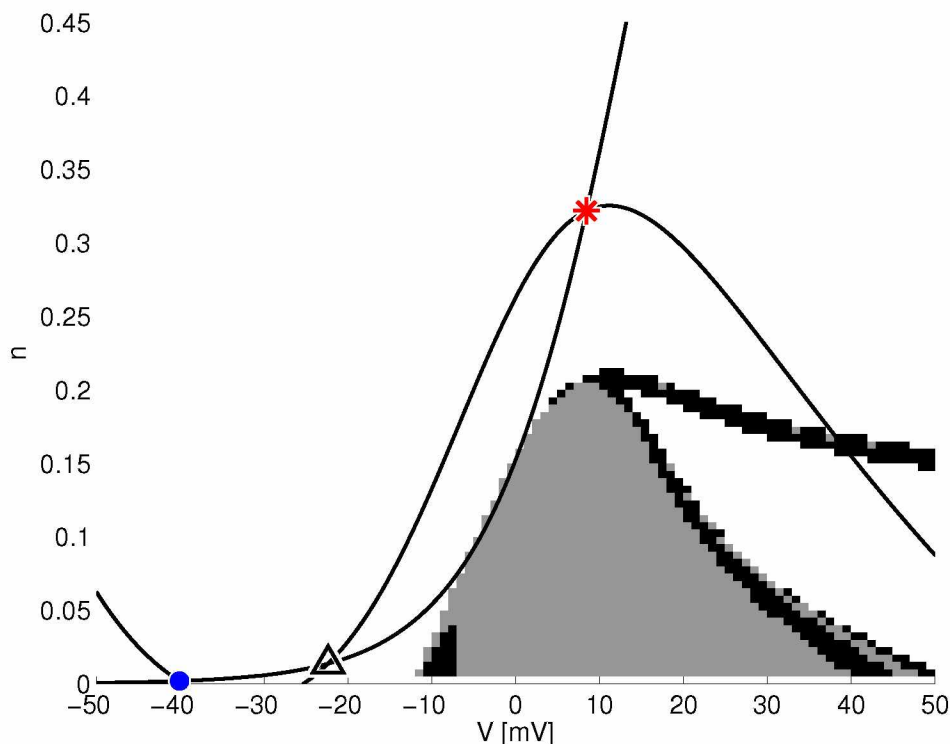

Figure 4.1. Instantaneous network state for a single input neuron in the Morris-Lecar system with $I_{app} = 35mA/cm^2$ for a 100-neuron network. Phase portrait of the membrane potential, V, against the channel occupancy state, n. Each discrete point, (V, n) describes a set of initial conditions. The instantaneous state of the network, $L = 1000ms$ later, is represented by the color of the pixel at each point, (V, n) with a resolution of $(\Delta V, \Delta n) = (2.0mV, 0.01)$. The dark grey represents a steady state, black and light grey represent a chaotic and a pulse state respectively.

When a single neuron in a resting network is perturbed (Figure 4.3, $d = 0$), the network dynamics can escape the steady-state attractor for perturbations in the region $\frac{dV}{dt} > 0$ and
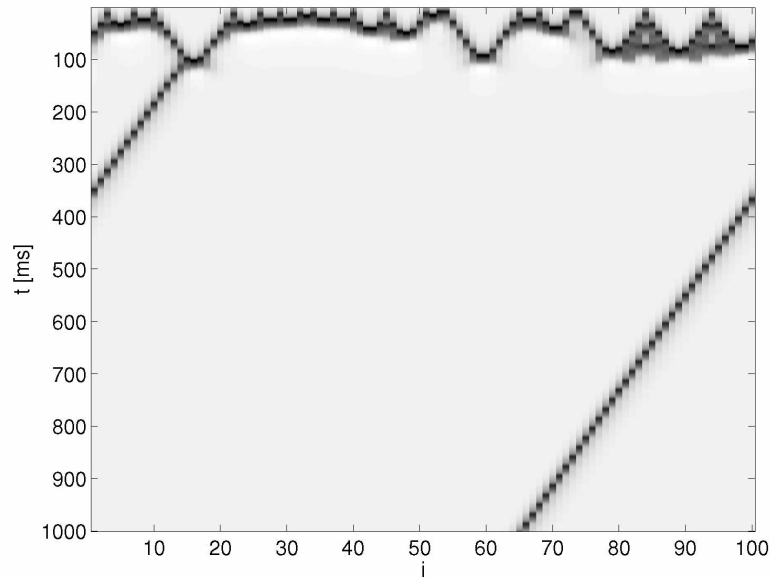
Figure 4.2. Bypassing transient chaos. Spatiotemporal dynamics for a 100-neuron network. A network at the resting potential is perturbed by a set of randomly-selected input neurons leading immediately to a pulse solution. See Figure 3.1 for details

$\frac{dn}{dt} > 0$. For low I_{app}, this region is small, running parallel to the V-nullcline; the majority of trajectories in this region make a transition directly to the pulse state. For medium applied currents, it becomes more likely that the perturbation will lead trajectories into the region of the chaotic saddle. For higher I_{app}, pulse states become more prevalent. Though the boundaries between state regions appear to be simple, a finer sampling of the phase space at these borders reveals more complicated structures at finer scales, appearing as striatal layers parallell to the boundary. Structure boundaries appear to lie perpendicular to a typical trajectory of a single excited neuron in phase space (dotted line in Figure 2.1). Transforming the Morris-Lecar system to polar coordinates (r, θ) and placing the focus at the origin, boundary transitions occur more as a function of θ than r. Treatments of the Morris-Lecar system with only a θ dependency have been successful at modeling features such as parabolic bursting[49].

The single input study demonstrates how a single input neuron can, with sufficient perturbation, drive the network into another state. For a given neural network in the brain there could be several simultaneous perturbations acting on the network from various
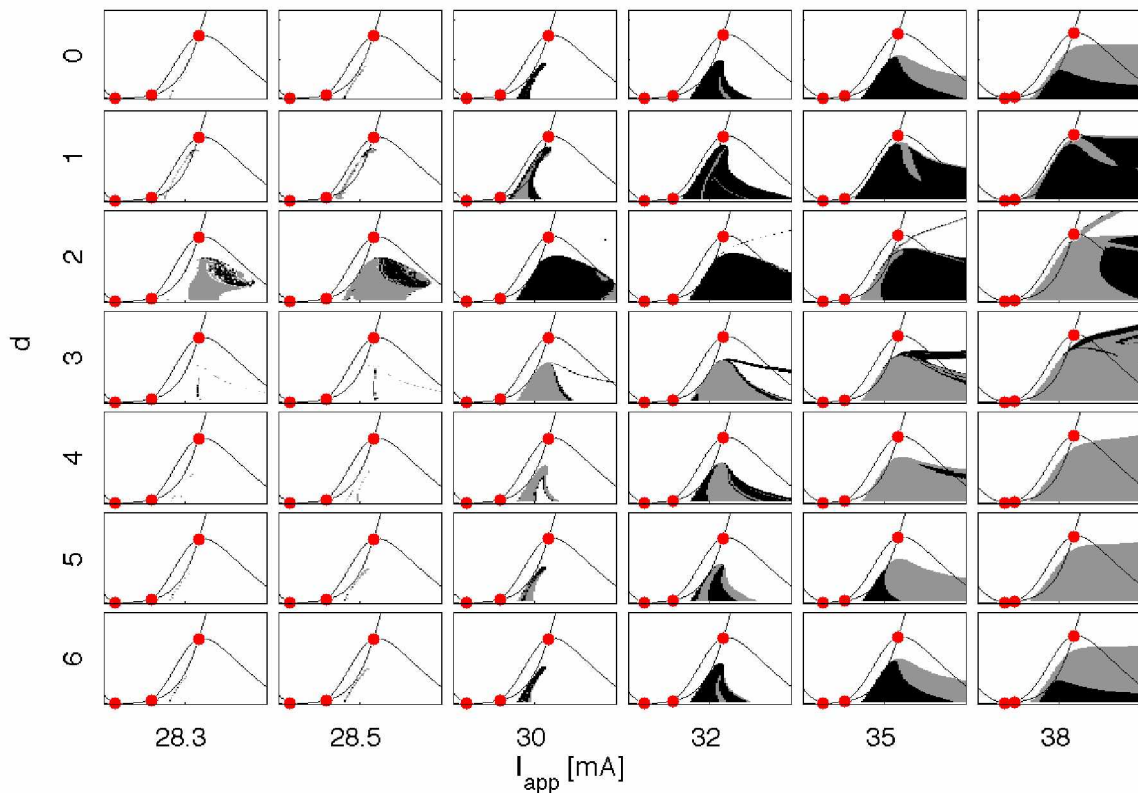
Figure 4.3. Two input neurons. Instantaneous network states as a function of the distance between input neurons, d, and the applied current, I_{app}. For technical details about individual axes, see Figure 4.1. Initial condition scheme: $d = 0$ represents a single input neuron in a network of neurons at the resting potential. For $1 \geq d \geq 7$, two input neurons are selected at the appropriate phase point, separated spatially by d.

environmental stimuli. To develop this idea, a second input neuron is added to aid in understanding interference between two synchronous stimuli. Both neurons are perturbed to the same point in phase space but separated spatially in the network by a distance of d neurons for $1 \leq d \leq 6$. As d approaches 6, the emergent structures in the basin-like plots begin to mimic the single-input result ($d = 0$).

Averaging over all d, larger applied currents provide more paths to the chaotic state than lower applied currents. For the majority of perturbations with low I_{app}, the system returns quickly to the steady-state attractor, but for $d = 2$, in which the perturbations are more likely to result in transient chaos across the whole range of applied current. For low

I_{app} and $d = 2$, the basin-like structures are complicated and scattered with the majority of perturbations kicking the network into the pulse state. For $I_{app} \geq 30mA/cm^2$, structures continue to grow and develop branches as I_{app} is increased. Within these growing structures of INSs that do not immediately reach the steady-state, pulse states becomes more typical than the chaotic state. Ignoring steady-state results, initial conditions with longer distances and larger applied currents tend to lead to a pulse-state outcome, while shorter distances with a large applied current tend to result in a chaotic state.

The third and final study on the network at rest utilizes *three* input neurons for the initial conditions (Figures 4.4, 4.5, and 4.6). For each I_{app}, the location of three input neurons can be represented by their two nearest distances in the ring network. For small distances in a large ring network, the distances are interchangeable as they always remain well below half of the total network size. Thus, for any pair of distances, the relatively smaller distance, d_s, is interchangeable with the relatively larger distance, d_l. $(d_l, d_s) = (2, 1)$ results in the same dynamics as $(d_l, d_s) = (1, 2)$.

In many aspects, results from the two-input study can inform the three-input study. For instance, at low I_{app}, structures resulting from $d = 2$ in the two-input study correspond to $d_s = 2$ in the three kicker study. For any given d_l, the shape of the basin-like structures do not vary significantly as long as $d_s = 2$ (Figure 4.4). However, some configurations produce new structures not available in the two-input study, such as $(d_l, d_s) = (2, 1)$ and $(d_l, d_s) = (6, 3)$. For a medium current, the two-input study is similarly preserved; this is particularly clear for $d_l = 7$. As $d_l \rightarrow 1$, new structures begin to emerge from the interference between input neurons. The shorter distance, d_s, tends to determine the overall shape of the basin-like structures with d_l making small alterations to the structure. For instance, when $d_s = 3$, increasing d_l changes the ratio of chaotic states to pulse states, but the structure representing steady states experiences no significant change (Figure 4.5). Similar observations hold for $I_{app} = 35$. For all currents, in the cases $d_l \leq 3$, structures change unpredictably as a result of the spatial interference at small distances.

The study on the network at rest gives insight into the perturbation characteristics that lead the system dynamics away from the attractor, giving some indication of the strength of the attractor. When the perturbation is distributed in space (multiple input neurons) smaller spatial distances ($d_s \leq 2$) have a higher chance of inducing transient chaos.
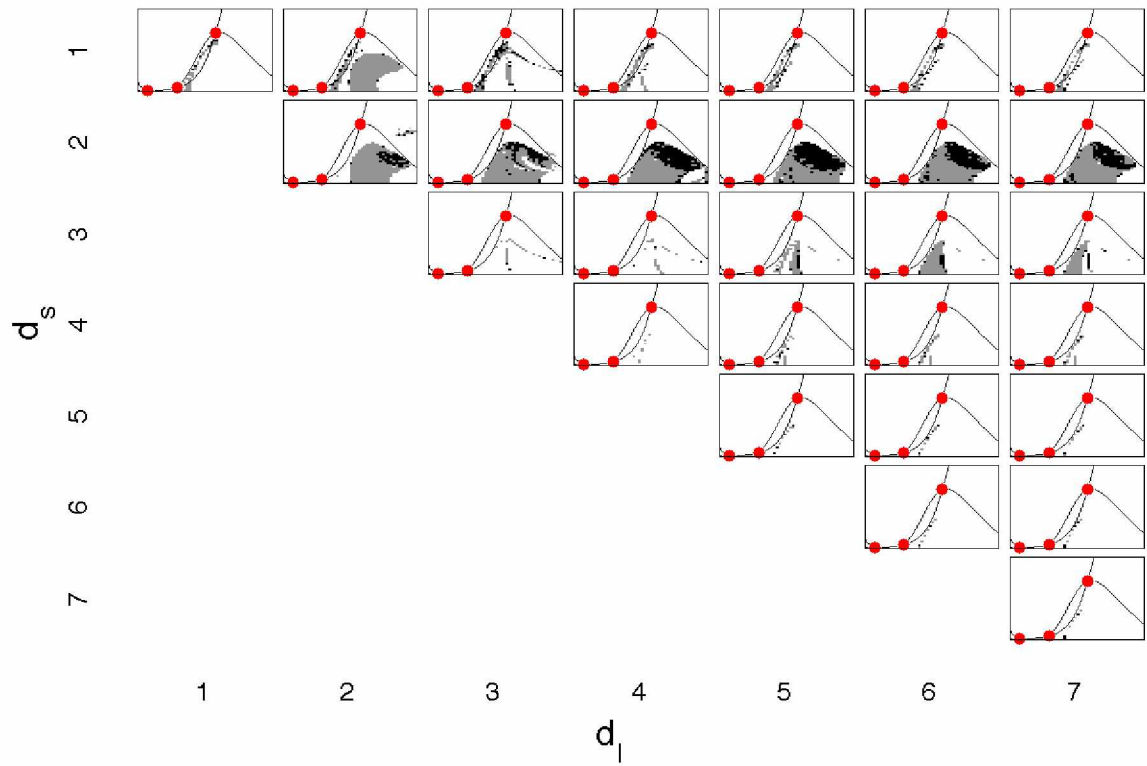
Figure 4.4. Three input neurons, $I_{app} = 28.5 mA/cm^2$. Basin-like plots with three input neurons for an applied current of $28.5mA/cm^2$ with varying distances, d_l and d_s. See Figure 4.1 for more details.

Figure 4.5. Three input neurons, $I_{app} = 28.5mA/cm^2$. Basin-like plots with three input neurons for an applied current of $32mA/cm^2$ with varying distances, d_l and d_s. See Figure 4.1 for more details.

Figure 4.6. Three input neurons, $I_{app} = 28.5mA/cm^2$. Basin-like plots with three input neurons for an applied current of $35mA/cm^2$ with varying distances, d_l and d_s. See Figure 4.1 for more details.
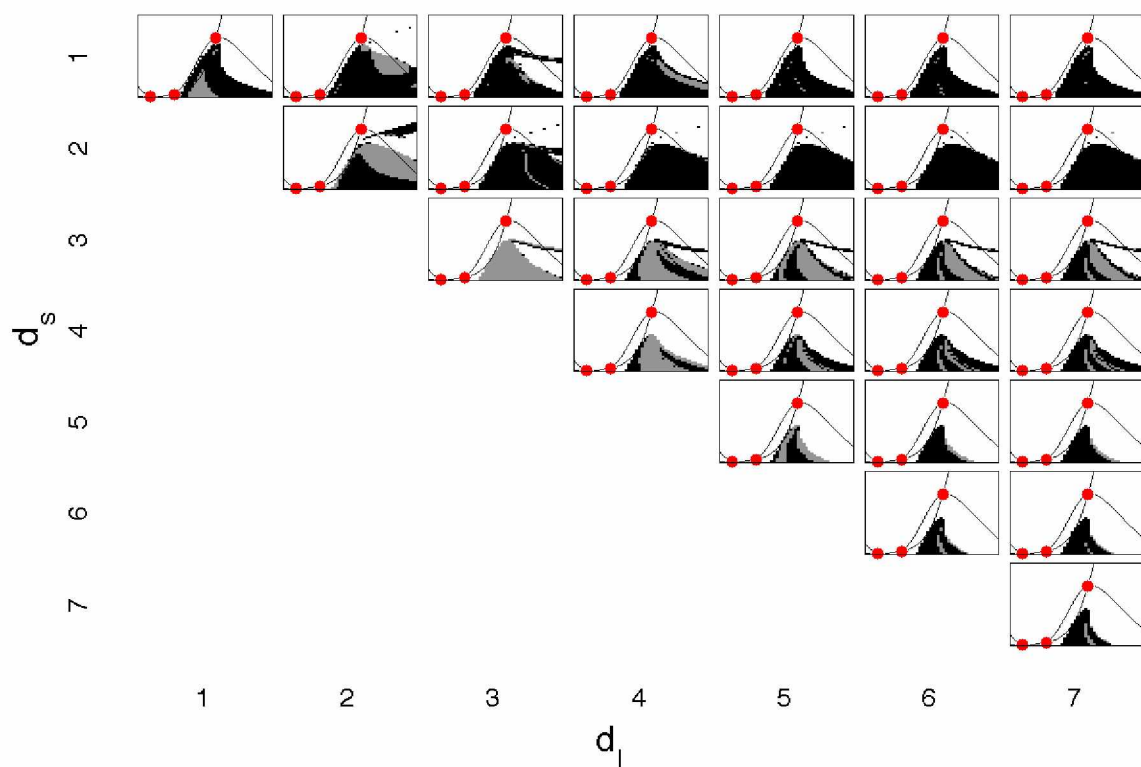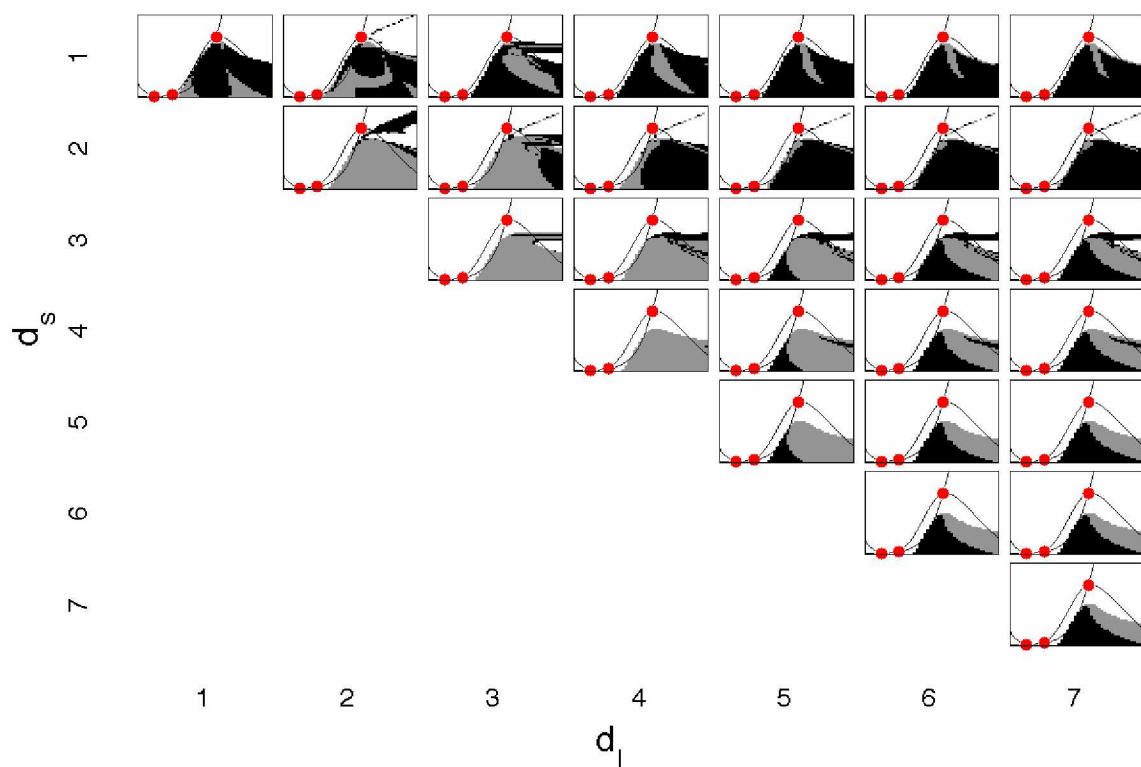
Chapter 5

Perturbations on a network in the neighborhood of the chaotic saddle

The Morris-Lecar system can undergo long-lived transients prior to collapse. As discussed in Chapter 3, the average lifetime of such transients increases with the applied current, I_{app}, but predicting when collapse occurs remains obscured by the complexity of high-dimensional interactions. Long periods of spatiotemporal chaos, followed by a collapse to an attractor with with negative Lyapunov exponent, indicate the existence of a chaotic saddle. In an effort to understand the robustness of network dynamics, perturbations are introduced to the network while it is in a transient chaotic state, presumably in the neighborhood of the chaotic saddle.

Ten transient chaotic states are chosen for each value of applied current, such that in the absence of perturbation, the network dynamics would continue in a state of transient chaos for at least 1000ms. For each chaotic state, P neurons in a 100-neuron network are randomly selected to provide synchronous input to the network. The input neurons are simultaneously set to each position in a projected, two-dimensional phase space and the network evolves deterministically for 1000ms before being measured.

In a 100-neuron network, P is equivalent to the percentage of the network perturbed. For $P = 0$, there are no perturbations, and the network remains in the chaotic state for the duration of the sample time. For low P and high applied current, the chaotic state results from the majority of perturbations in the two-dimensional phase space (Figure 5.1). For $P \in [33, 66]$, the phase space becomes disjected and intricate structures emerge as multiple states are measured across the projected phase space. In this medium perturbation regime, low currents sometimes result in the familiar structure from $I_{app} = 28.5, d_s = 2$ in the network at rest (Figure 4.4); particularly, $(I_{app}, P) = (28.3mA, 33)$. With increasing current at medium perturbation, causing collapse with a perturbation becomes increasing difficult, especially for perturbations near the unstable focus. As the fraction of perturbation neurons is increased further, collapse become inevitable, with the exception of a small region parallel to the $V - nullcline$, between the saddle-node and the unstable focus $((I_{app}, P) = (30mA, 90))$. For higher currents, the focus itself continues to be a region where perturbations do not promote the collapse of spatiotemporal chaos $((I_{app}, P) = (38mA, 90))$.

A statistical analysis is compiled from the basin plots, taking the average occurence
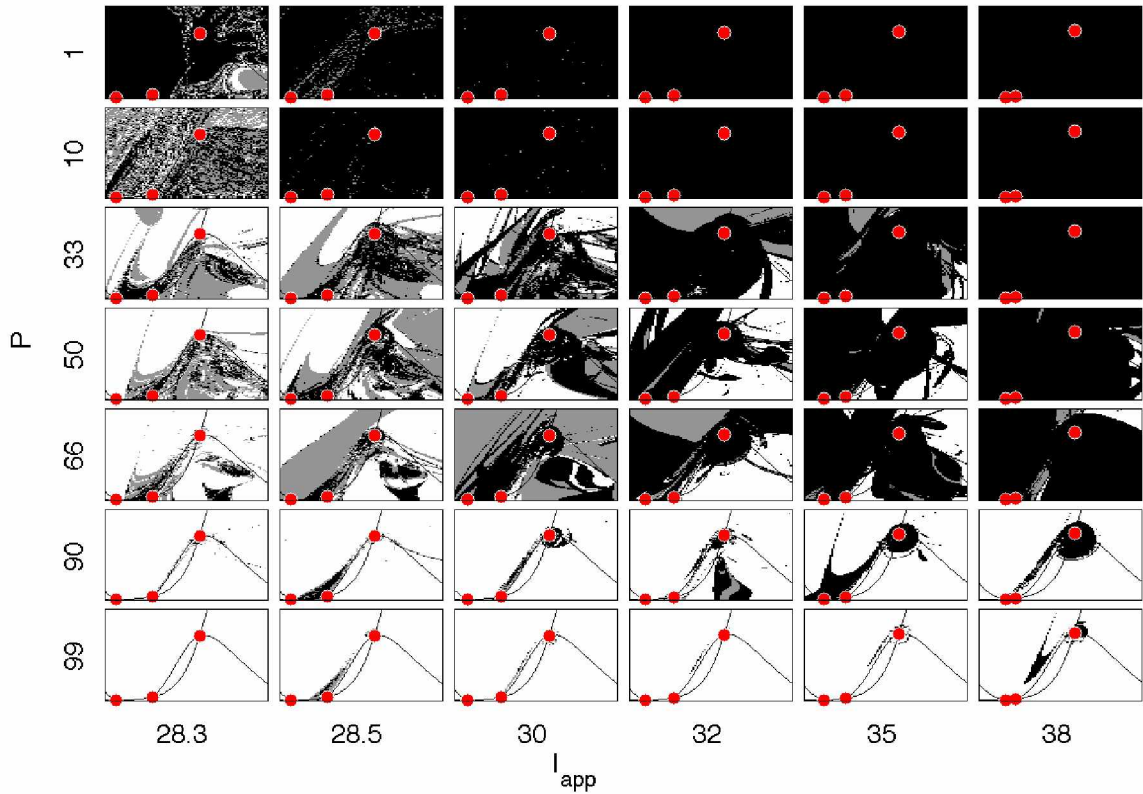
Figure 5.1. Perturbations near the chaotic saddle. Examples of instantaneous network state maps as a function of the applied current, I_{app} and the number of perturbing neurons, P. Ten randomly selected perturbation sets are delivered to ten randomly selected chaotic sets. Of these 100 trials, for each value of I_{app} and P, one randomly-selected example is shown. For details on each network state map, see 4.1

of each of the three instantaneous states as a function of I_{app} and P. From this data, the probability of a perturbation-induced collapse, p_C is defined as the average fraction of trials for which trajectories reached the steady-state or the pulse state within 1000ms of the perturbation. Increasing the applied current generally reduced the probabiliy of a collapse response to perturbations, but as P approaches 100, $p_C \to 1$ (Figure 5.2a). At lower currents, such as $I_{app} = 28.5 mA/cm^2$, p_C has a distributed result as a function of P. Higher currents demonstrate threshold behavior in which network dynamics resist collapse unless a minimum P is provided. The probability of a collapse to pulse state, p_P, is similarly calculated over I_{app} and P. The probability of collapse to a pulse state holds no significant

relationship with applied current (Figure 5.2b). However, a larger number of synchronized perturbations are less likely to cause a collapse to the pulse state.
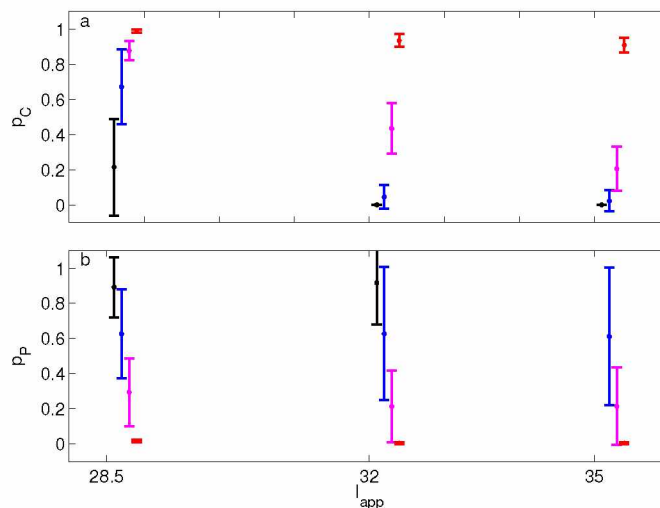

Figure 5.2. Instantaneous network statistics. a) The probability of a perturbation-induced collapse, p_C, and b) The probability of a collapse to the pulse state, p_P, as a function of applied current, I_{app}, and number of perturbed neurons, P, with $P=10,30,50$, and 90 (offset to the right). For $(I_{app}, P) = (35mA/cm^2, 10)$, p_P is undefined since $p_C = 0$. Statistics compiled from network state maps. See Figure 5.1 for technical details.

The collapse of transient chaos to a pulse state indicates the existence of a homoclinic orbit. The trajectory of a single neuron in a network in the pulse-state was projected onto the two-dimensional phase space of a single neuron (Figure 5.3, pulse state). Pulse-state trajectories pass through the stable fixed point with each excitation cycle. A neuron in a network in the chaotic state demonstrates the full range of behavior described in Chapter 3 (Figure 3.2). As the applied current is increased, trajectories caught in the neighborhood of the unstable focus tend to make larger orbits near the focus, despite its eigenvalue approaching zero (Figure 5.3, chaotic state).

Perturbations lying along the V-nullcline (Figure 2.1) where $\frac{dn}{dt} < 0$ almost never cause a collapse in the network dynamics in the time-scale of measurement ($1000ms$). This is particularly evident for a large number of perturbing neurons ($P \geq 90$) in which this region of phasespace, along with a region around the focus, remain chaotic through the measurement period. The region of excitation ($\frac{dV}{dt} > 0$ and $\frac{dn}{dt} > 0$) that before induced chaos
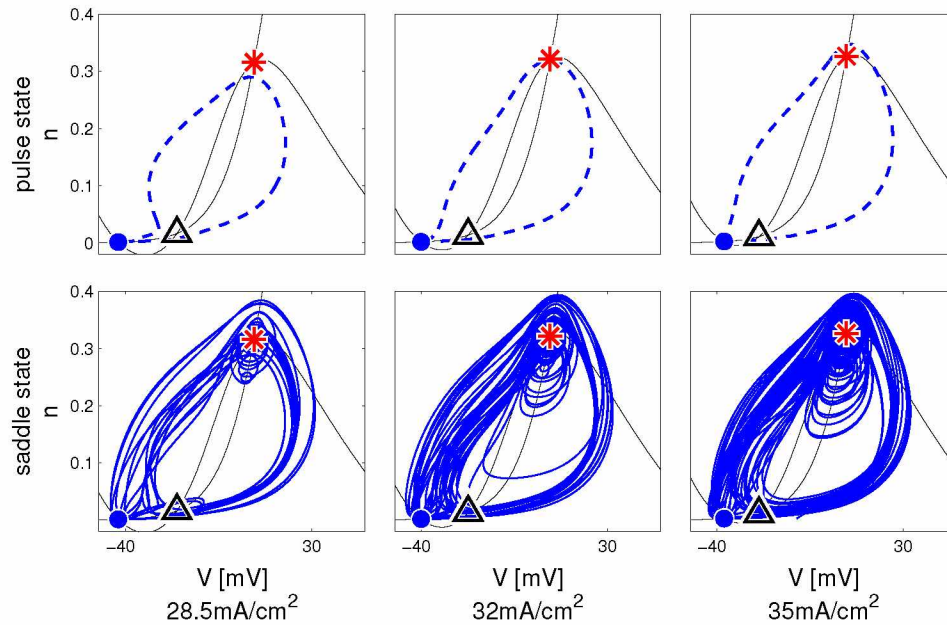
Figure 5.3. Homoclinic and chaotic orbits. Typical trajectories for a single neuron in the coupled network in the pulse state (above) and the chaotic state (below) for $I_{app} = 28.5mA/cm^2, 32mA/cm^2$, and $35mA/cm^2$. Nullclines are plotted as lines with the unstable focus (asterisk), saddle point (triangle) and stable point (filled circle) at their intersections.

in the network at rest (Chapter 4) now has a tendency to collapse a chaotic network to the steady-state (such as in Figure 5.1, $P = 66, I = 28.3mA/cm^2, 28.5mAcm^2$, and $32mA/cm^2$). These basin-like plots provide a map for facilitating the collapse of transient spatiotemporal chaos in a ring network of Morris-Lecar neurons, but may also give insights into general control mechanisms for coupled excitable systems.

Chapter 6

Conclusions

Transient spatiotemporal chaos was found in the diffusively coupled Morris-Lecar ring network with three available attractors: the steady-state, the pulse solution and, in special cases of applied current, the chaotic attractor. Trajectories escaping the neighborhood of the chaotic saddle deterministically reach the attractors with no external perturbation. Dislodging the dynamics from the attractor states requires superthreshold perturbations for a network on the steady-state or a pulse attractor, but the trajectories are easily dislodged from the chaotic attractor with arbitrarily small perturbations (Figure 6.1).

The lifetime of transient chaotic behavior increases exponentially with the size of the network as well as the applied current. Statistical and graphical analysis of initial conditions demonstrate consistent regions of excitability for which chaos can be induced in a network at rest. Similar analysis reveals for which perturbations an early collapse of spatiotemporal chaos to an attractor can be facilitated.
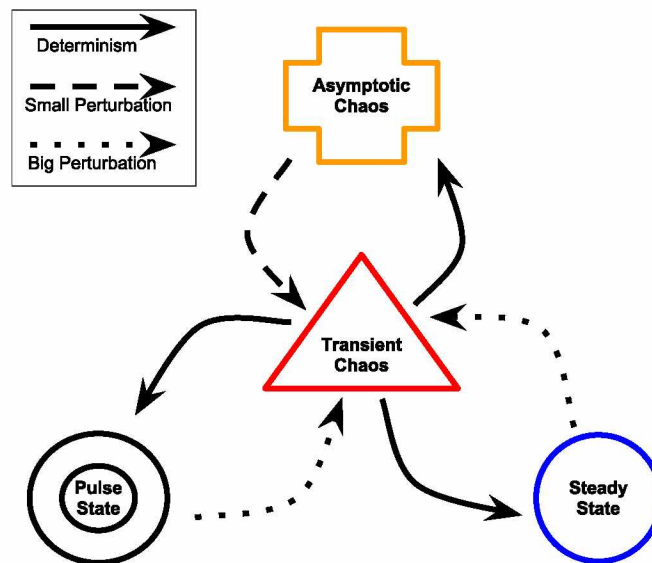
Figure 6.1. A generalized state map for the Morris-Lecar ring network. The dynamics of the system can reach all three attractors deterministically from the transient chaotic state. From the steady state or the pulse-state, a significant perturbation is required to induce transient chaos, while arbitrarily small perturbations on the chaotic attractor can induce transient chaos. The chaotic attractor becomes available when $I_{app} = 38$. Paths between the attractors are not shown.

Computational roles of gap junctions in neural network

Axo-axonic gap junctions connect nearby axons in nervous tissue, allowing molecular and electrical signaling to propagate between neuronal axons in the absence of dendritic input. In the mammalian brain, axo-axonic gap junction networks in the hippocampus are hypothesized to be associated with memory consolidation. Due to their fast transmission speed, they are able to quickly synchronize networks and have been indicated in spontaneous and self-sustained synchronous oscillations. Axo-axonic gap junction networks have a unique mechanism for signaling, as they allow signals to travel antidromically (up the axon) or laterally to parallel neurons, allowing for signal processing to occur independent of synaptic input[42]. This has implications for the capibility of axo-axonic gap junctions to participate significantly in neural computations in the brain beyond their traditionally accepted role in synchronization[38]. The existence of spatiotemporal chaos in the Morris-Lecar ring network demonstrates that holding synaptic input and environmental conditions constant in a network of electrically coupled axons can lead to complex transient behavior.

Machine Learning

The phase space of the Morris-Lecar neural network demonstrates distinct regions of network excitability to a chaotic state as well as regions of transition between attractor states. The ability to induce, as well as facilitate the collapse of, transient chaos allows for such a network to be integrated as a layer in a learning network in which the axon layer can act as an input or hidden layer, receiving stimuli. For example, consider each Morris-Lecar neuron in the ring-network as an inhibitory or excitatory neuron, determined by its synaptic output to a motor pool (Figure 6.2). Information about the environment enters the network via input neurons, as well as through feedback connections from the network's output. Using a genetic algorithm, the network can be tuned to respond appropriately to environmental stimuli to produce a functional control system.
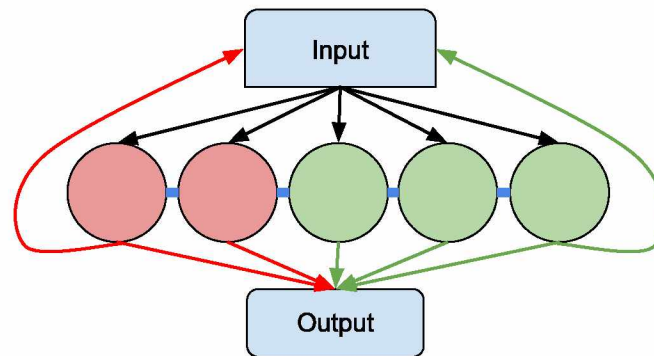
Figure 6.2. Machine learning network. An input signal is delivered to the electrically coupled (blue lines) Morris-Lecar ring network. Morris-Lecar neurons can be excitatory (green) or inhibitory (red) and synaptic outputs can be modeled to produce and output signal that can excite (green lines) or inhibit (red lines) downstream, as well as provide feedback to the network input.

Boundary conditions in the nervous system

In natural gap junction networks, boundary conditions are regularly controlled by internal cell processes. Gap junctions can be opened, closed, and rectified in response to the appropriate signaling mechanisms between neighboring cells. For sufficiently large ring networks, or when no-flux boundary conditions are applied to the Morris-Lecar system, oscillations drift quickly across the network, converging with and diverging from neighboring oscillating clusters. For small, bound ring networks ($N < 500$), where sensitivity to initial conditions is dependent on network size, boundaries created by the opening and closing of gap junctions could have functionally relevant results.

The asymptotic chaotic state is a result of a very specific set of boundary conditions. Perturbations on a Morris-Lecar network experiencing asymptotic chaos lead trajectories quickly to the neighborhood of the chaotic saddle, initiating complex transient dynamics before terminating on one of the three attractors in the system. Linking the resulting attractor state to a particular gating configuration could be a way to implement algorithmic sequences in network dynamics.

6.1 Outview

The presented complexity of a diffusively-coupled Morris-Lecar network opens the door to further possible studies. The parameter region above the saddle-node bifurcation where a stable limit cycle exists exhibits rich oscillatory dynamics. Modification of the coupling constant influences the pervasiveness and speed of traveling pulse solutions. Changes to both parameters result in spatiotemporal structures that appear qualitatively different than those in the excitable regime. An understanding of how the coupling constant and applied current affect global network properties beyond the regions explored here could aid in controlling network dynamics.

Similarly, the scope of the instantaneous network states investigated here can be expanded to include finer sampling, more initial conditions, and longer time-scales. Preliminary results show that information is generated with finer sampling of the phase space, causing boundaries between basin-like structures to become ill-defined and fractal-like. Of the possible configurations of initial condition available, very few have been investigated here. Since the basin-like plots are defined for finite time and include non-attractor states, these structures will change with time, until all trajectories reach a steady-state and a true basin of attraction can be defined. A time-lapse perspective of the basin-like plots could give insights into collapse processes.

The addition of a synaptic coupling term to the ring network can have dramatic effects on network outcome. Synaptic coupling can be either inhibitory or excitatory, allowing for a fixed input that can influence network outcome. Through feedback connections, inhibitory and excitatory signals can be used to modulate the degree of activity in the network, keeping target neurons below (or above) threshold when the controlling neuron is active. Synaptic coupling in the nervous system can facilitate more robust network responses.

Manipulations to network topology can give insight into how control systems in the nervous system use gap junction gating to influence network behavior. A sufficiently large neural network could, hypothetically, use gating to partition subnetworks into functional compartments, directing signal propagation on the fly. Gap junction gating in the nervous system can be triggered by neurotransmitters as well as functionally diverse free-radical gasses like nitrogen oxide.

Bibliography

[1] H. Wilson. *Spikes, decisions, and actions: the dynamical foundations of neuroscience.* Oxford University Press, USA, 1999.

[2] H. D. Abarbanel and M. I. Rabinovich. *Current Opinion in Neurobiology,* 11(4):423 – 430, 2001.

[3] E. Izhikevich. *Dynamical systems in neuroscience: the geometry of excitability and bursting.* Computational Neuroscience. MIT Press, 2006.

[4] P. Dayan and L. Abbott. *Theoretical neuroscience: computational and mathematical modeling of neural systems.* Computational Neuroscience. MIT Press, 2005.

[5] G. Ermentrout and D. Terman. *Mathematical foundations of neuroscience.* Interdisciplinary Applied Mathematics. Springer, 2010.

[6] E. Schwartz. *Computational neuroscience.* System Development Foundation Benchmark Series. MIT Press, 1993.

[7] M. I. Rabinovich and P. Varona. *Frontiers in Computational Neuroscience,* 5(24), 2011.

[8] W. Becker. *The world of the cell.* Benjamin/Cummings series in the life sciences. Benjamin/Cummings Pub. Co., 1986.

[9] J. Byrne and J. Roberts. *From molecules to networks: an introduction to cellular and molecular neuroscience.* Academic Press/Elsevier, 2009.

[10] R. Parsons. *Journal of Electroanalytical Chemistry and Interfacial Electrochemistry,* 278(12):441 – 442, 1990.

[11] A. L. Hodgkin and A. F. Huxley. *The Journal of Physiology,* 117(4):500–544, 1952.

[12] C. Morris and H. Lecar. *Biophysical Journal,* 35(1):193 – 213, 1981.

[13] S. Strogatz. *Nonlinear dynamics and chaos.* Sarat Book House, New York, 1994.

[14] Y. Lai and T. Tél. *Transient chaos: complex dynamics on finite time scales.* Applied Mathematical Sciences. Springer, 2011.

[15] S. Smale, M. Hirsch, and R. Devaney. *differential equations, dynamical systems, and an introduction to chaos*. Pure and Applied Mathematics. Elsevier Science, 2003.

[16] D. Egolf, I. Melnikov, W. Pesch, and R. Ecke. *Nature*, 404(6779):733–6, 2000.

[17] K. He. *Phys. Rev. E*, 59:5278–5284, 1999.

[18] Q. Ouyang and J.-M. Flesselles. *Nature*, 379:143–146, 1996.

[19] R. Wackerbauer and S. Kobayashi. *Phys. Rev. E*, 75:066209, 2007.

[20] S. Yonker and R. Wackerbauer. *Phys. Rev. E*, 73:026218, 2006.

[21] R. Wackerbauer and K. Showalter. *Phys Rev Lett*, 91:174103, 2003.

[22] R. Wackerbauer. *Phys. Rev. E*, 76(5):056207, 2007.

[23] S. Wolfram. *Physica D: Nonlinear Phenomena*, 10(1-2):1–35, 1984.

[24] K. J. Painter and T. Hillen. *Physica D: Nonlinear Phenomena*, 240(45):363 – 375, 2011.

[25] H. Malchow, F. Hilker, R. Sarkar, and K. Brauer. *Mathematical and Computer Modelling*, 42(910):1035 – 1048, 2005.

[26] J. Sprott. *Nonlinear Dynamics, Psychology, and Life Sciences*, 16(4):387–95, 2012.

[27] J. Bascompte and R. V. Sole. *Trends in Ecology and Evolution*, 10(9):361 – 366, 1995.

[28] S. V. Petrovskii and H. Malchow. *Theoretical Population Biology*, 59(2):157 – 174, 2001.

[29] H. Fujii and I. Tsuda. *Neurocomputing*, 5860(0):151 – 157, 2004.

[30] M. Wang, Z. Hou, and H. Xin. *ChemPhysChem*, 7(3):579–582, 2006.

[31] W. Mao-Sheng, H. Zhong-Huai, and X. Hou-Wen. *Chinese Physics*, 15(11):2553, 2006.

[32] X. Xin-li and W. Wan-liang. In *Proceedings of the 4th World Congress on Intelligent Control and Automation, 2002*, volume 3, pages 1749 – 1753, 2002.

[33] L. Chen and K. Aihara. *Neural Networks*, 8(6):915–930, 1995.

[34] A. Wacker, S. Bose, and E. Schöll. *EPL (Europhysics Letters)*, 31(5-6):257, 1995.

[35] D. Stahlke and R. Wackerbauer. *Phys. Rev. E*, 80:056211, 2009.

[36] D. Stahlke and R. Wackerbauer. *Phys. Rev. E*, 83:046204, 2011.

[37] B. W. Connors and M. A. Long. *Annual Review of Neuroscience*, 27(1):393–418, 2004. PMID: 15217338.

[38] E. Leznik and R. Llins. *Journal of Neurophysiology*, 94(4):2447–2456, 2005.

[39] R. Publio, R. F. Oliveira, and A. C. Roque. *PLoS ONE*, 4(9):6970, 2009.

[40] F. K. Skinner, L. Zhang, J. L. P. Velazquez, and P. L. Carlen. *Journal of Neurophysiology*, 81(3):1274–1283, 1999.

[41] A. Draguhn, R. Traub, D. Schmitz, and J. Jefferys. *Nature*, 394(6689):189–192, 1998.

[42] D. Feldmeyer and J. Lübke. *New aspects of axonal structure and function.* SpringerLink: Springer e-Books. Springer, 2010.

[43] K. Tsumoto, H. Kitajima, T. Yoshinaga, K. Aihara, and H. Kawakami. *Neurocomput.*, 69(4-6):293–316, Jan. 2006.

[44] G. Benettin, L. Galgani, and J.-M. Strelcyn. *Phys. Rev. A*, 14:2338–2345, Dec 1976.

[45] Y. Kuramoto and I. Nishikawa. *Journal of Statistical Physics*, 49:569–605, 1987. 10.1007/BF01009349.

[46] O. Mazor and G. Laurent. *Neuron*, 48(4):661 – 673, 2005.

[47] D. Durstewitz and G. Deco. *Eur J Neurosci*, 2007.

[48] M. Stopfer, V. Jayaraman, and G. Laurent. *Neuron*, 39(5):991–1004, 2003-09-11 00:00:00.0.

[49] G. Ermentrout and N. Kopell. *SIAM Journal on Applied Mathematics*, 46(2):233–253, 1986.